



**HAL**  
open science

# Synthesis of superacid sulfated TiO<sub>2</sub> prepared by sol-gel method and its use as a titania precursor in obtaining a kaolinite/TiO<sub>2</sub> nano-hybrid composite

Carlos Rafael Silva de Oliveira, Marcos Antonio Batistella, Antônio Augusto Ulson de Souza, Selene Maria de Arruda Guelli Ulson de Souza

## ► To cite this version:

Carlos Rafael Silva de Oliveira, Marcos Antonio Batistella, Antônio Augusto Ulson de Souza, Selene Maria de Arruda Guelli Ulson de Souza. Synthesis of superacid sulfated TiO<sub>2</sub> prepared by sol-gel method and its use as a titania precursor in obtaining a kaolinite/TiO<sub>2</sub> nano-hybrid composite. Powder Technology, 2021, 381, pp.366-380. 10.1016/j.powtec.2020.11.063 . hal-03109809

**HAL Id: hal-03109809**

**<https://imt-mines-ales.hal.science/hal-03109809>**

Submitted on 6 Jun 2023

**HAL** is a multi-disciplinary open access archive for the deposit and dissemination of scientific research documents, whether they are published or not. The documents may come from teaching and research institutions in France or abroad, or from public or private research centers.

L'archive ouverte pluridisciplinaire **HAL**, est destinée au dépôt et à la diffusion de documents scientifiques de niveau recherche, publiés ou non, émanant des établissements d'enseignement et de recherche français ou étrangers, des laboratoires publics ou privés.

# Synthesis of superacid sulfated TiO<sub>2</sub> prepared by sol-gel method and its use as a titania precursor in obtaining a kaolinite/TiO<sub>2</sub> nano-hybrid composite

Carlos Rafael Silva de Oliveira<sup>a,\*</sup>, Marcos Antonio Batistella<sup>b</sup>,  
Antônio Augusto Ulson de Souza<sup>a</sup>, Selene Maria de Arruda Guelli Ulson de Souza<sup>a</sup>

<sup>a</sup> Federal University of Santa Catarina, Chemical Engineering Department, Mass Transfer Laboratory, PO Box 476, Florianópolis, SC 88.040-900, Brazil

<sup>b</sup> IMT Mines Alès, Polymers Composites and Hybrids (PCH), 6, Avenue de Clavières, Alès 30319, France

## ABSTRACT

Superacid sulfated TiO<sub>2</sub> was prepared by the sol-gel method and tested as a titania precursor to obtaining a kaolinite/TiO<sub>2</sub> nano-hybrid composite. Raman, FTIR, Zeta Potential, and XRD analyses allowed the identification of kaolinite and titania as well as the interactions between them to form the nanohybrid composite. SEM-FEG/TEM analyses clearly showed titanium nanocrystals adhered to the surface of kaolinite microparticles. Thermogravimetric analysis of the powders showed that the composite obtained has a tenuous thermal reinforcement due to the presence of TiO<sub>2</sub>. Furthermore, the composite has excellent photocatalytic activity, reaching up to about 97% of methylene blue degradation under UV-C radiation in 3 h. Therefore, this study proposes a simple, safe, and effective method for the use of sulfated TiO<sub>2</sub> as a precursor in the synthesis of composite nanomaterials based on titania.

### Keywords:

Kaolinite  
Titanium dioxide  
Nano-hybrid composite  
Sulfated TiO<sub>2</sub> sol-gel  
Methylene blue  
Photocatalytic activity

## 1. Introduction

Nanosized oxides, such as ZnO, Fe<sub>2</sub>O<sub>3</sub>, Al<sub>2</sub>O<sub>3</sub>, SnO<sub>2</sub>, SiO<sub>2</sub>, and Bi<sub>2</sub>O<sub>3</sub> have attracted much attention in recent years due to their photocatalytic properties [1–4] and have been used in various applications as water treatment [5], adsorption of heavy metals [6,7], photodegradation of dyes [8], among others. Titanium dioxide (TiO<sub>2</sub>), in addition to its photocatalytic properties, has been explored due to its additional properties, such as antimicrobial [9], self-cleaning [10], semiconductors [1], optics [1] and photocatalytic activity [4,7,11]. However, for some applications, the nanometric size combined with the polar characteristics of the crystals can cause some drawbacks in the use of this material, an example is the high recovery cost of TiO<sub>2</sub> nanopowders when used for photocatalytic treatments of residues [12]. To overcome these drawbacks, the immobilization of TiO<sub>2</sub> nanoparticles on supports [12] like kaolinite, bentonite, vermiculite, and others [12–15] have been evaluated.

De Almeida et al. [16] and Noda et al. [17] synthesized and studied a sulfated TiO<sub>2</sub> and successfully applied the material as a reaction catalyst in the methanolysis of soybean and castor oils, and the

isomerization of n-hexane. Titania is a very stable metal oxide and under neutral conditions of pH, temperature, and pressure can be considered an inert material. However, when sulfated, it becomes an oxide with very high acidity, becoming a superacid solid [16–20]. In order to evaluate the acidity of superacid solids, a Hammett acidity function (H<sub>0</sub>) was proposed and is widely accepted [21,22]. The Hammett acidity function was first used to measure the acidity of highly concentrated solutions of strong acids and in the study of organic reactions catalyzed by strong acids [23]. In 1927, Hall and Conant [24] suggested the use of the term superacid and Gillespie [25] proposed an arbitrary, but widely accepted definition of superacids, as any system that achieves a stronger acidity compared to a 100% sulfuric acid solution, *i.e.*, with H<sub>0</sub> ≤ −12. Fluorsulfuric and trifluoromethane sulfonic acids are considered superacids with H<sub>0</sub> values of −15 and −14.1, respectively [23]. To achieve the acid values of a superacid, a system of conjugated strong acids is normally using a strong acid (Brønsted acid) (Eq. (1)).



When a strong Lewis acid is added to a strong Brønsted acid, a shift in the Brønsted acid autoprotolysis balance occurs due to the formation of an HA acid counterion, the LA<sup>−</sup> anion is more delocalized (Eq. (2)).

\* Corresponding author.

E-mail address: carlos.oliveira@posgrad.ufsc.br (C.R.S. de Oliveira).



Obtaining a superacid solid can be done in two ways, increasing the intrinsic acidity of an acidic solid by adding another acid or supporting a superacid liquid in a solid (which can be acidic or not) [23]. Between materials that are used as superacid solids ( $Al_2O_3$ ,  $TiO_2$ ,  $SiO_2$ ,  $Fe_2O_3$ ,  $ZrO_2$ ,  $ZnO$ ) titania has been widely studied because of its chemical properties [2,16–18,23]. Super acidity of sulfated titanium is attributed to the Brønsted acid sites created in titania by the high sulfate content increasing the acidity of the solid by the presence of strong Lewis acid sites in its vicinity. The strength of Lewis acidic sites is related to the inductive effect of sulfate on the metallic atom (titanium atom), which becomes more electron-deficient and takes the form of a cation ( $Ti^{n+}$ ) [2,3,17–19,26]. The sulfation of titania acts as an activator of the oxide enabling the bonding of titania into the surface of the supports, like clays [13,16–18,23].

The immobilization of titania in the surface of clay minerals gives rise to nanostructured materials with excellent photocatalytic properties. These materials have been widely explored in research that apply these composites in the removal of organic compounds by advanced oxidative processes [1,13,27–31]. Various clay minerals have been used as a support for  $TiO_2$  nanoparticles. Among them, kaolinite offers some advantages because they can undergo acid activation and become reactive and highly adsorptive. Kaolinite is a hydrated aluminum silicate, its structure is of the 1:1 type with stoichiometric formula  $Al_2Si_2O_5(OH)_4$  [32–35]. The structure of kaolinite is formed by a layer of silicon tetrahedrons adjacent to an octahedral aluminum layer, strongly bonded by hydrogen bonds [32–35]. Studies of the chemical behavior of surface have shown that kaolinite has a preferentially negative electrical charge, mainly in the exposed basal planes. According to Doi et al. [36], Sposito et al. [35], Murray [37] and Leroy et al. [38] most clay minerals acquire a specific surface charge in aqueous solution. According to Doi et al. [36] and Sposito et al. [35], kaolinite presents two types of surface potential, permanent and dependent. The permanent surface potential is negative, and it is attributed to the isomorphous substitution of  $Si^{4+}$  by  $Al^{3+}$  in the tetrahedral plane. The dependent surface potential has an amphoteric character, *i.e.*, it depends on the pH of the medium, and is located on the edges of the crystal, which acquire positive (protonation) or negative (deprotonation) charges. This behavior can be explained by the presence of imperfections of the crystal, such as cracks, broken edges, and states of high amorphization [35–39]. According to Bergaya and Lagaly [40], Brady et al. [41] and Liu et al. [42] lateral surface and edges of the kaolinite crystal are highly reactive due to the abundance of amphoteric OH groups (donors/recipients). However, the basal surface (silanol and aluminum sites) is less reactive than the edges because of the lower concentration of OH groups. Moreover, ionization reactions promote the deprotonation of the edges or the protonation and hydroxylation of the basal surface [36,40–42].

The physicochemical characteristics of kaolinite (ion exchange capacity, adsorbance of metal cations, high surface area, porosity, non-toxicity, chemically inert) allow the adhesion of various oxides on the surface of the mineral [1,13]. However, the studies reported in the literature that aims to obtain silicate/ $TiO_2$  composites use titanium precursor compounds that are admittedly expensive and hazardous, factors that hinder the large-scale industrial production and commercialization of these photocatalyst composites [1]. In most works tetrabutylorthotitanate ( $C_{16}H_{40}O_4Ti$ ), Titanium (IV) tetraisopropoxide ( $C_{12}H_{28}O_4Ti$ ), Titanium oxychloride ( $TiOCl_2$ ), Titanium tetrachloride ( $TiCl_4$ ) are used, sometimes with other surfactants or organic solvents to improve the final result [1,12,13,43]. Therefore, in the present work, the obtention of a sulfated  $TiO_2$  by superacid sol-gel and its grafting onto the kaolinite surface was evaluated in replacing other commercial precursors for the preparation of a nano-hybrid composite.

## 2. Experimental section

### 2.1. Materials

Kaolinite (PK) under the trade name Saca-B® was kindly donated by IMERYS do Brasil Comércio de Extração de Minérios Ltda. Titanium dioxide under the trade name AEROXIDE®  $TiO_2$  P25 was obtained by Evonik do Brasil Ltda. Sulfuric Acid 98% and Methylene blue P.A. (C.I. 52.015) were purchased from LabSynth Ltda (Brazil), and Absolute Ethyl Alcohol 99.8% was purchased from Neon Ltda (Brazil). All reagents were used as received.

### 2.2. Experimental procedure

The methodology used in this research occurs in two steps. The first step consists in the preparation of a sulfated  $TiO_2$  by the sol-gel method using a modified methodology, which was first proposed by Noda et al. [17] and De Almeida et al. [16]. To perform the synthesis, 61 mL of distilled water and 15 g of AEROXIDE®  $TiO_2$  P25 were slowly mixed under constant magnetic stirring for 30 min in a beaker. After that, the beaker containing the mixture was kept in a container with ice under vigorous magnetic stirring, and 30 mL of sulfuric acid ( $H_2SO_4$ ) was slowly added into the titania suspension, and maintained for 30 min under magnetic stirring, as shown in Fig. 1. After acid addition, the suspension was kept under constant stirring at 80 °C for 1 h and 30 min. At the end, a white and gelatinous aqueous dispersion (sol-gel) was obtained. Sol-gel was reserved in amber glass and kept at room temperature.

The second step consists in grafting  $TiO_2$  into the kaolinite crystals to obtain the nano-hybrid composite material. A 500 mL jacketed glass reactor was fitted with a condenser on a magnetic stirrer and connected to a digital ultra-thermostatic bath (SL-152, Marconi) with temperature control. 200 mL of distilled water and 20 g (10% w/v) of kaolinite (PK) Saca-B® were added to the reactor. The mixture was kept under constant stirring and the medium temperature was raised to 90 °C. Upon reaching 90 °C, 50 mL (25% v/v) of the titanium sol-gel (previously prepared) were slowly dripped through one of the nozzles of the reactor cover. After adding the titanium sol-gel to the reaction medium, the system was maintained at 90 °C for 24 h. After it, the reaction medium was left until complete solids decanting. At room temperature, the final pH of the supernatant was measured and pH values  $\leq 1.0$  were found. The solid material was washed five times with distilled water and the supernatant was discarded. Finally, KT particles were filtered using a 0.21  $\mu m$  PTFE (Teflon) membrane. The KT composite was washed and filtered until the wash water had a conductivity lower than  $1 \cdot 10^2 \mu S/cm$ , in order to ensure that all sulfate ions were removed. Fig. 1 illustrates the process of obtaining the KT composite. The KT composite was dried at 50 °C for 3 h in a laboratory oven. After drying, the solid was easily milled with the help of a porcelain pistil and reserved in an amber glass container.

To compare the photocatalytic activity of the obtained powder (KT) by the proposed method, the same synthesis procedure was conducted with the use of pure kaolinite (PK) and AEROXIDE®  $TiO_2$  P25 as received (*i.e.*, without previous sulfation of the  $TiO_2$ ), to obtain a secondary powder called KT\*.

### 2.3. Structural and microstructural characterization

The surface charges of  $TiO_2$ , PK, and KT were investigated by Zeta Potential measurements. For all analyses, the samples were tested in triplicate at room temperature ( $\sim 25$  °C), with dispersion in distilled water and pH variation from about 1.0 to 12.0. The Zeta Potential readings were performed on a ZetaSizer Nano-ZS (Malvern Instruments Ltd.) equipment.

Fourier transform infrared spectroscopy was used to analyze the particles in KBr pellets on a Cary 660 FTIR Spectrometer (Agilent

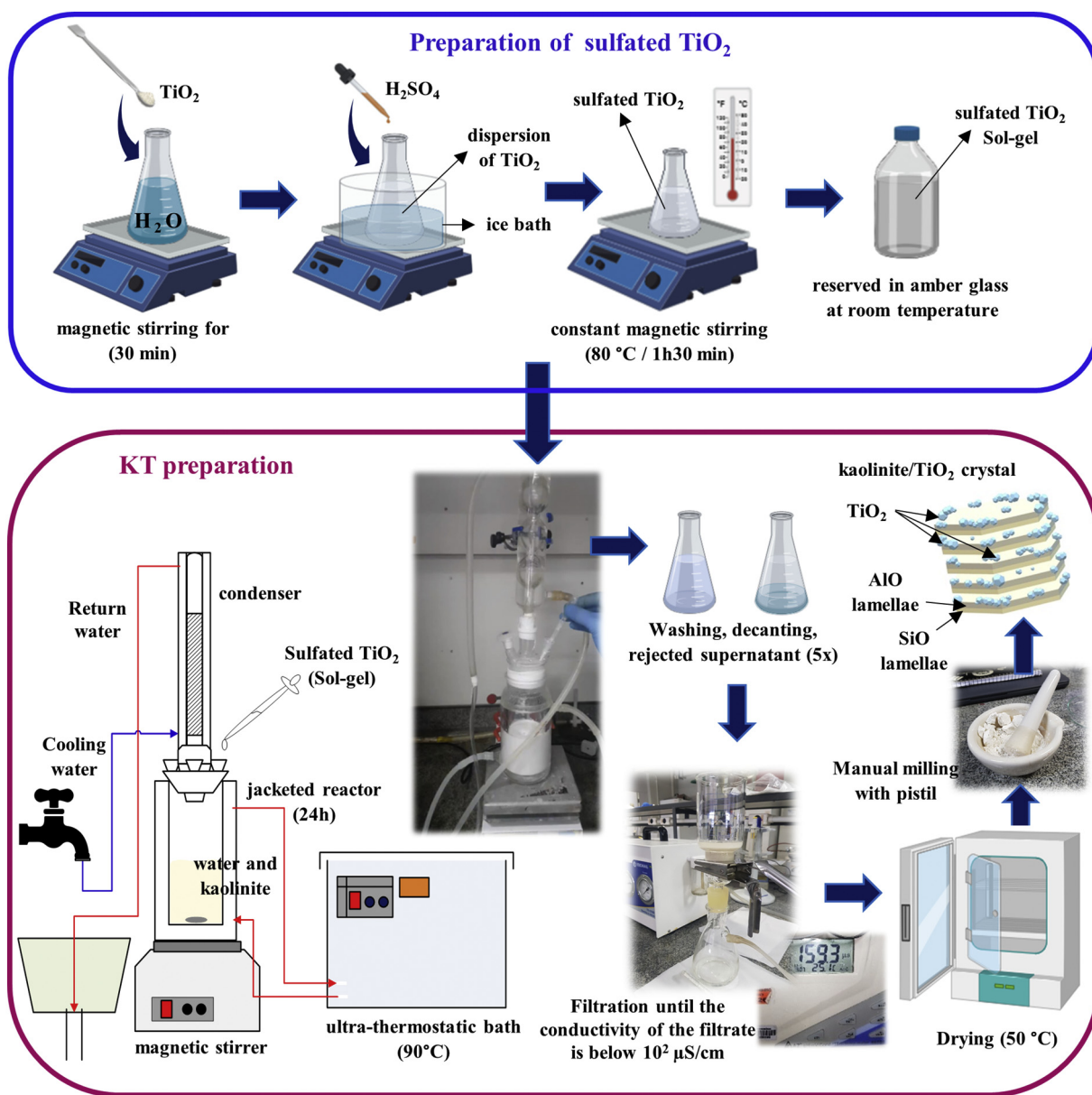


Fig. 1. Schematic illustration of the experimental procedure for preparing the sulfated  $\text{TiO}_2$  and KT composite.

Technologies) equipment, with readings in the region of  $4000\text{--}400\text{ cm}^{-1}$ , with a resolution of  $2\text{ cm}^{-1}$ .

Raman spectra were measured with Cora 5 × 00 Raman Spectrometer (Anton Paar), using a Raman laser of 785 nm and 400 mW, with spectral reading in the region of  $100\text{--}2000\text{ cm}^{-1}$ , and the step length of  $2\text{ cm}^{-1}$ .

UV-vis DRS (Diffuse Reflectance Spectroscopy) analyses of KT composite and  $\text{TiO}_2$  was carried out using a Lambda 45 UV-vis Spectrometer (Perkin Elmer) equipment, the absorption of the materials was obtained in the region from 200 to 700 nm.

The morphology and microstructures of commercial  $\text{TiO}_2$ , sulfated  $\text{TiO}_2$ , PK particles, and KT composite were characterized by Scanning Electron Microscopy-FEG using a JSM-6701F (Jeol Ltd.), and by Transmission Electronic Microscopy using a JEM-1011 (Jeol Ltd.) equipment.

The particle size readings of PK and KT by Dynamic Light Scattering (DLS) were performed using a MasterSizer 3000 (Malvern Instruments Ltd.), and the  $\text{TiO}_2$  particle size readings were carried out on a ZetaSizer Nano-ZS (Malvern Instruments Ltd.) equipment. Before analysis, the

particles were dispersed for 5 min in distilled water using a USC-1400 ultrasonic bath (Unique Ltda.).

The X-Ray Diffraction (XRD) analysis was carried out on the MiniFlex600 X-ray Diffractometer (Rigaku Ltd.) equipment under radiation  $\text{Cu-K}\alpha$  ( $\lambda = 0.154\text{ nm}$ ) operated at 40 kV and 100 mA. The particle samples were prepared as pressed powders and data were collected under scan angle of  $2\theta$  from  $5^\circ$  to  $80^\circ$ , with a step size of  $0.01^\circ$  (step time: 0.2 s).

The thermal behavior of the particles was investigated using a thermogravimetric analyzer Jupiter STA-449 F3 (Netzsch, Germany), in the TGA-DTG analyses the particles were heated from room temperature to  $800\text{ }^\circ\text{C}$  with a heating rate of  $10\text{ }^\circ\text{C}/\text{min}$  under synthetic air atmosphere, with a flow rate of 20 mL/min.

#### 2.4. Photocatalytic activity

The photocatalytic activity of the KT composite was evaluated in the degradation of the methylene blue dye (MB), using a modified

methodology adapted from ISO 10678: 2010 [44]. The photoreactor consisted of a black chamber (without external light input) equipped with a high-intensity UV-C radiation lamp (Osram Puritec HNS G5,  $P = 8 \text{ W}$ ,  $\lambda = 254 \text{ nm}$ ,  $\phi = 7800 \text{ cd}$ ,  $E_{\text{UV-C}} = 20 \text{ W/m}^2$ ) located in its upper part. Before the test, 0.15 g of powder (test sample) was left in a dark chamber for 24 h with 100 mL of 20 ppm aqueous MB solution (conditioning solution). This step is needed because the samples tend to adsorb the dye. After conditioning, the adsorption solution was replaced by the test solution (100 mL; 10 ppm) and was kept 15 cm away from the lamp and left in the dark for 10 min under stirring at 475 rpm. After that, the suspension was exposed to UV-C light for 3 h at room temperature ( $25 \pm 2 \text{ }^\circ\text{C}$ ) under the same stirring. Photocatalytic kinetics was evaluated at 20 min intervals by UV-vis absorption spectroscopy using the Q898U2M5 Microprocessor UV-VIS Spectrophotometer (Quimis Ltda.) equipment in the region from 400 to 750 nm, with a cell length of  $d = 10 \text{ mm}$ , and step of reading of 1 nm. For this, 50 mL of the sample have been taken and centrifuged (10,000 rpm; 5 min) in order to separate the solids. Next the supernatants were analyzed on UV-vis at 664 nm, then mixed and returned to the test solution to minimize the variation in volume. For comparison, the effect of light (photolysis), free AEROXIDE®  $\text{TiO}_2$  P25, and  $\text{KT}^*$  on MB photodegradation were tested. The PK effect was also tested, but only the initial and final absorption were measured after 3 h of exposure to UV-C light. The reference sample (blank) was kept in the dark and the UV-vis absorption was also measured at the same period of time.

### 3. Results and discussion

#### 3.1. Structural and thermal characterization of the particulated materials

##### 3.1.1. Zeta potential analyses

Fig. 2a shows the results of Zeta Potential measurements of pure kaolinite (PK), titania and composite kaolinite/ $\text{TiO}_2$  (KT). For the PK in the pH range of 1.0–12.0, the Zeta Potential is negative, and the isoelectric point (IEP) of the clay mineral was not observed in agreement with some results in literature [45–52]. According to Shankar et al. [50], silica and alumina sheets in kaolinite have permanent negative charge sites, induced by isomorphous substitutions. Furthermore, the silica sheet is normally negative for pH values above 2.0, while the alumina sheet is pH-dependent and can reach IEP at  $\text{pH} \pm 9.5$ . Moreover the net charge at the edge of the particle can be negative or positive, depending on pH [50]. According to Shankar et al. [50] and Au et al. [49], the edge-to-face

area ratio can determine different kaolinite charge behavior as a function of the pH. This implies that the basal surface of the negatively charged (permanent) particle dominates the surface properties and can explain the behavior observed [49–51].

The  $\text{TiO}_2$  particles showed positive Zeta Potential values for the pH range below 6.0. Between pH 6.0 and 6.5 the titanium IEP was found, i.e., at this pH, the suspension becomes unstable, since the neutrality of the particles induces the agglomeration formed by intermolecular forces of the dipole-dipole type and hydrogen bonds. From pH 6.5, the particles acquire a negative charge and the electronegativity of the particles continuously increases to a pH close to 9.0. Above pH 9.0, the suspension becomes stable and the particles tend to remain dispersed by electrostatic repulsion. According to Liao et al. [53] and Xu et al. [54], the Zeta Potential of titanium nanoparticles in aqueous suspension depends on factors such as pH, particle morphology (crystalline arrangement and surface area) ion concentration and ion charge. In the presence of a strong electrolyte, the oxides undergo hydration and form reactive amphoteric hydroxyl groups on the exposed surface. In aqueous solutions containing diluted electrolytes, the titania surface acquires surface charges by reacting with the  $\text{H}^+$  and  $\text{OH}^-$  ions present or added to the medium. Interaction of the hydroxyl groups with the ions in solution will determine the surface charge and the Zeta Potential of the suspension, as shown in equation (Eq. (3)).



The results are in agreement with the literature, where the same behavior as a function of pH and approximate IEP value for  $\text{TiO}_2$  was observed [55,56]. It can be observed that for pH values below 2.0, the KT particles have a positive surface character and IEP was about  $\text{pH} \pm 2.0$ . From pH values above 2.0, the particles become more electronegative and tend to be dispersed by electrostatic repulsion effects. Curves of PK and KT have very similar behavior, this indicates that although there are changes promoted by the presence of titanium in KT, the composite is formed mostly by kaolinite, and therefore the electrokinetic behavior of the material is similar to the PK.

##### 3.1.2. FTIR analyses

The FTIR results of PK,  $\text{TiO}_2$ , and KT composite are shown in Fig. 2b. Various absorption bands related to hydroxyl groups can be observed. Peaks in the region between  $3800$  and  $3000 \text{ cm}^{-1}$  shows an intense

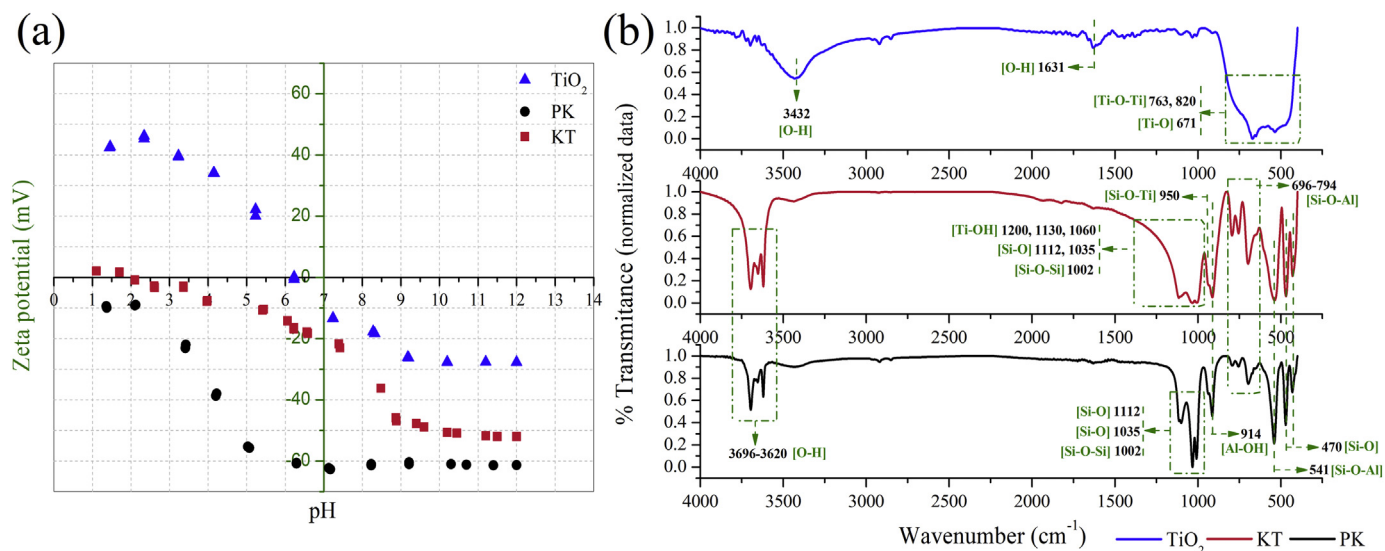


Fig. 2. (a) – Zeta Potential analysis of  $\text{TiO}_2$ , KT composite, and PK. (b) – FTIR analysis of  $\text{TiO}_2$ , KT composite, and

band corresponding to the stretching of the hydroxyl group "O-H", and the peak at  $1631\text{ cm}^{-1}$  can be related to the deformation vibrational mode "H-O-H". For both bands, the hydroxyl group can be attributed to the presence of absorbed water in the sample [57,58]. Moreover, it is possible to notice a high-intensity peak between  $800$  and  $450\text{ cm}^{-1}$ , characteristic of "Ti-O" stretching vibration [57,58].

For PK and KT the absorption peaks at  $3696$ ,  $3670$  and  $3652\text{ cm}^{-1}$  correspond to the "O-H" bond stretching of the internal (interlayer) kaolinite surface, studied by Ledoux and White [59]. The peaks at  $3620$  and  $914\text{ cm}^{-1}$  are also related to the stretching mode of the "OH" bond, however in this case the hydroxyl groups are related to those presents in the empty places of the crystal, as reported by Hess and Saunders [60] and Valášková et al. [61]. Peaks at  $1112$  and  $1035\text{ cm}^{-1}$  can be related to "Si-OH" deformation vibrations of the kaolinite silanol groups, present in the basal and lateral planes of the particles according to Makó et al. [62]. Peaks at  $790$  and  $541\text{ cm}^{-1}$  correspond to the translational vibrations "OH" and deformation of the "Al-O-Si" bonds, respectively. Finally, the peak at  $1002\text{ cm}^{-1}$  concerns "Si-O-Si" non-symmetrical stretching vibrations of kaolinite siloxane bonds [52,63].

The FTIR spectrum of KT composite shows some differences compared to PK samples. The peaks between  $400$  and  $900\text{ cm}^{-1}$  of the spectra are a strong indicator of the presence of  $\text{TiO}_2$  and can be attributed to stretching vibration of "Ti-O". The broad peak that appears between  $1200$  and  $900\text{ cm}^{-1}$  may be owing to the superposition of "Ti-O", "Si-O", and "Al-O" bonds. The peak observed at  $950\text{ cm}^{-1}$ , which can be assigned to "Si-O-Ti" antisymmetric stretching vibration, suggests the chemical combination of titania and kaolinite to the formation of KT composite. The broad peak including the bands at  $1060$ ,  $1130$  and  $1200$  belonging to bending vibration of "Ti-O-H" in the anatase phase. [1,12,13,43,64].

### 3.1.3. Raman analyses

Raman spectroscopies of PK,  $\text{TiO}_2$ , and KT composite are shown in Fig. 3. PK spectrum presents a characteristic peak at  $141\text{ cm}^{-1}$  that corresponds to the symmetric bending modes of the "O-Al-O" and "O-Si-O" of kaolinite and/or halloysite [65–67]. The halloysite band at  $200\text{ cm}^{-1}$  refers to the vibrations of the  $\text{AlO}_6$  octahedron [66]. The kaolinite bands at  $246\text{ cm}^{-1}$  and dickite at  $276\text{ cm}^{-1}$  are related to a mixture of "Si-O" deformation with "OH" and  $\text{AlO}_6$  octahedral sheet vibrations,

respectively [66]; they can also be related to the "OH-O" vibrational modes [68]. The kaolinite bands at  $334$ ,  $390$ ,  $430$ ,  $464$ , and  $514\text{ cm}^{-1}$  are attributed to bending vibration of "O-Si-O", while the strong band at  $637\text{ cm}^{-1}$  is related to hydroxyl (Al-OH) translational vibration [68]; the peak at  $514\text{ cm}^{-1}$  can also be attributed to the vibrations of the "Si-O-Al" group [66]. The nacrite band at  $711\text{ cm}^{-1}$  and kaolinite at  $750$  and  $791\text{ cm}^{-1}$  are associated with the vibration and translation modes of "Al-O-Si", and some of which involves structural OH [65,66]; while the band of dickite and/or kaolinite in  $914\text{ cm}^{-1}$  is assigned to the "Al-OH" deformation mode.

$\text{TiO}_2$  and KT spectra revealed the characteristic anatase band at  $146$  and  $145\text{ cm}^{-1}$ , respectively, attributed to the "O-Ti-O" symmetric vibration mode [69,70]. The anatase phase has a very strong signal of Raman spectra, unlike the kaolinite which for the same band has weak Raman spectra, this is because Raman activity is related to the change in polarizability during vibration [69]. Besides, molecules and crystals with transition metals have a more covalent chemical character, and therefore provide more intense Raman bands, such as titanium (Ti), which is easily polarizable; unlike kaolinite which is composed of atoms of silicon (Si) and aluminum (Al) that are less polarizable, and therefore provide much weaker Raman bands [69].

It is possible to state that the band at  $145\text{ cm}^{-1}$  in the KT spectrum corresponds to the presence of the anatase phase, because the peak is much more intense than in the PK spectrum, this is due to the fact of the extreme sensitivity of the Raman to the high symmetry of the "O-Ti-O" vibration [69]. The  $\text{TiO}_2$  spectrum showed bands in  $198$ ,  $395$ ,  $514$ , and  $637\text{ cm}^{-1}$  associated with the vibrational modes  $E_g$ ,  $B_{1g}$ ,  $A_{1g}$ , and  $E_g$  of anatase, respectively [69–71]. The rutile band at  $443\text{ cm}^{-1}$ , corresponding to the vibrational mode of  $E_g$  was identified in the analyzed sample. In the KT spectrum, characteristic peaks of the matrix phase (kaolinite) of the composite were identified at  $334$ ,  $560$ ,  $725$ , and  $790\text{ cm}^{-1}$ , among other bands of clay minerals that compose the kaolin, such as the nacrite bands at  $250$  and  $988\text{ cm}^{-1}$ , dickite at  $847\text{ cm}^{-1}$ , and halloysite at  $944\text{ cm}^{-1}$ . The anatase bands at  $145$ ,  $394$ ,  $513$ , and  $638\text{ cm}^{-1}$  were also identified, which confirms the presence of the dispersed phase ( $\text{TiO}_2$ ) of the obtained composite.

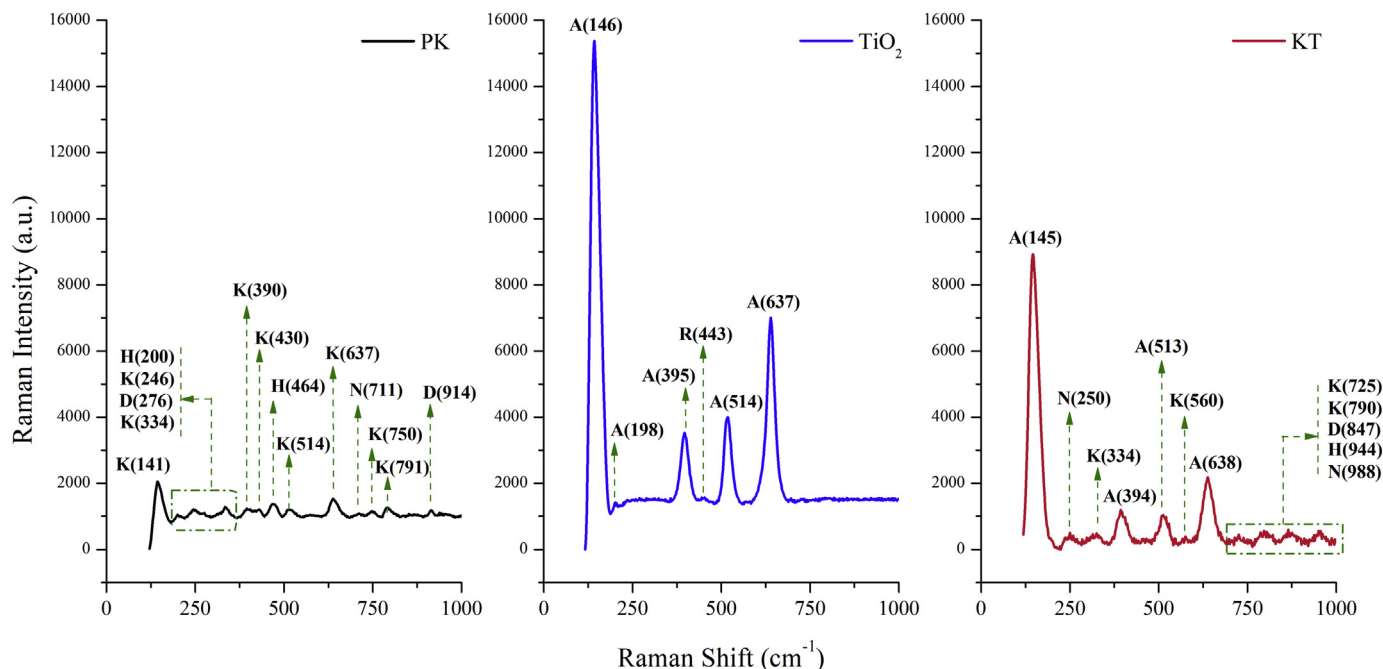


Fig. 3. Raman spectroscopy of  $\text{TiO}_2$ , KT composite, and PK.

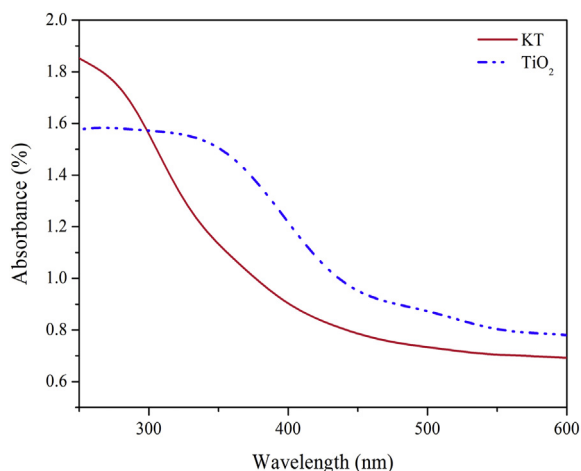


Fig. 4. UV-vis DRS of pure TiO<sub>2</sub>, and KT composite.

391 nm. The band energy for each material was calculated using Eq. (4), where  $E$  is the photon energy expressed in electron volts (eV),  $h$  is the Planck constant for eV whose value is  $4.136e^{-15}$  eV·s,  $c$  is the speed of light given by 299,792,458 m/s, and  $\lambda$  is the wavelength in meters (m).

$$E = \frac{h \cdot c}{\lambda} \quad (4)$$

The energy of the TiO<sub>2</sub> absorption bands and the KT composite showed the values of 2.91 and 3.17 eV respectively. This result suggests that kaolinite causes the displacement of the TiO<sub>2</sub> absorption edge to a region of greater energy. This increase in the band gap indicates that KT presents a more intense redox capacity compared to pure titania and, therefore, an improvement in the photocatalytic potential of the composite can be observed when applied for photocatalytic ends. The observed UV-vis results confirm the presence of titania adhered to the kaolinite and agree with the results found in the literature [1,4,12,13,43,72].

### 3.1.5. SEM-FEG and TEM analyses

Fig. 5 shows the micrographs of PK and KT samples. PK images revealed a flattened particulate material formed by the sequential stacking of hexagonal lamellae [73–75] with a high variation in particle size as well as the formation of clusters, which was confirmed by the DLS

### 3.1.4. UV-vis DRS analyses

UV-vis diffuse reflectance spectra of TiO<sub>2</sub> and KT composite are shown in Fig. 4. The spectra showed an absorption edge of TiO<sub>2</sub> at about 425 nm, while the absorption edge of KT composite was around

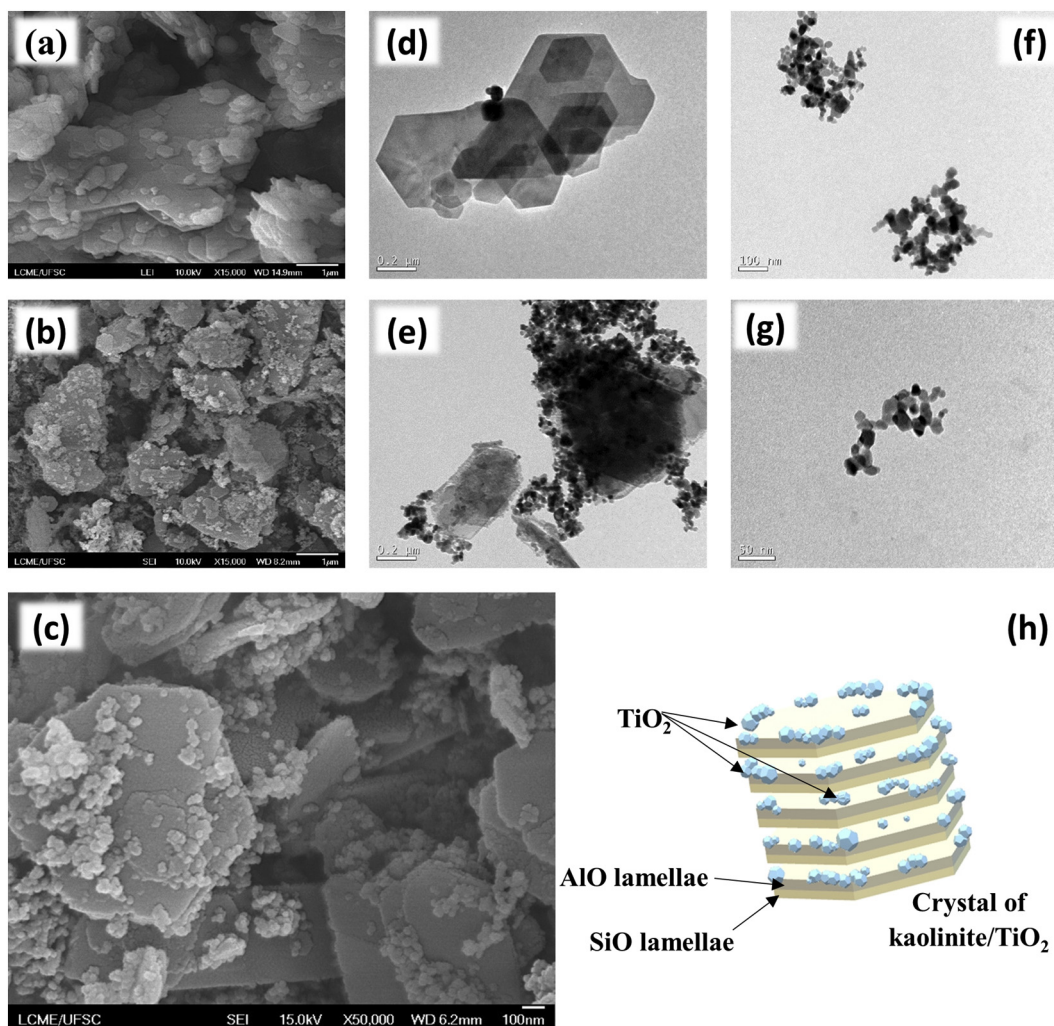


Fig. 5. SEM-FEG and TEM micrographs of the particles. (a) – Pure kaolinite (PK); (b) and (c) – Kaolinite/TiO<sub>2</sub> composite (KT); (d) – TEM of PK; (e) – TEM of KT; (f) – TEM of TiO<sub>2</sub>; (g) – TEM of Sulfated TiO<sub>2</sub>; (h) - Schematic representation of the crystal formation of KT composite.

analyses. KT composite micrographs revealed a material formed by kaolinite containing well distributed TiO<sub>2</sub> nanoparticles adhered to their surface. Titania was immobilized in the basal and lateral planes of the clay mineral in agreement with some results found in literature [1,12,30,43,76–78] and divergent from others [13,79]. Various studies have obtained different kaolinite/TiO<sub>2</sub> composites using different methodologies explaining the different morphologies obtained. Some researchers reported an anchorage of titania in the lateral hydroxyl sites of the kaolinite [13,79], while others showed the interaction of the oxide with the silicon atoms in the basal planes [1,12,43]. TEM images showed that the individual size of the TiO<sub>2</sub> particles are lower than 100 nm, with the formation of a nano-hybrid mixture formed between kaolinite and titania. Fig. 5f and g shows the TEM images of the commercial titania particles and the sulfated titanium dioxide, both of which appeared clustered. No morphological and size changes were observed between the materials.

### 3.1.6. DLS analyses

Fig. 6a and b show the histograms of particle size distribution for PK particles and KT composite. DLS analysis of PK revealed that about 10% (D10) of the particles are sub-micrometric (between 0.1 and 1 μm), as they have a diameter below 0.902 μm. At D50, an overall mean particle size value is 3.10 μm and indicates that 50% of the PK particles are below 3.10 μm. In D90, the size of 8.61 μm indicates that 90% of the particles has a particle size below 8.61 μm, probably formed by agglomerates.

For PK the highest particle diameter values of about 11.2 μm was observed, this identifies PK as a micrometric material (between 0.1 and 100 μm).

For the KT composite, DLS analysis revealed that up to 10% of the particles are sub-micrometric and have a diameter below 0.911 μm. In D50, the diameter was around 3.38 μm. However, D90 has a very large size of about 68.3 μm; but it was observed that the cumulative frequency in 85.5% of the material has a particle size of up to 8.68 μm. Therefore, about 85% of the sample has micrometric particles with a diameter below this size. The adhesion process of titania caused a change in the kaolinite particle size profile with an increase in the size of the particles and an increase in the generation of large agglomerates for KT compared to the results of PK. In addition to the increase in particle size, the composite showed greater variation and heterogeneity, which corroborates the trimodal distribution of the curve observed through the results of D90 and D99. Largest particle sizes found in the sample were around 586 μm, considered to be of macrometric size (above 100 μm), such particles represent a small percentage of the material and must be attributed to the formation of aggregates (agglomerates) generated in the obtaining reaction of the KT composite. Considering the high values of D90 and D99, as well as the discrepancy between their sizes, it is supposed that the growth rate of larger grains is much higher than that of the smaller particles. Such behavior can be partially explained by the heterocoagulation mechanism, which occurs for particles with opposite charges for the same pH condition. An

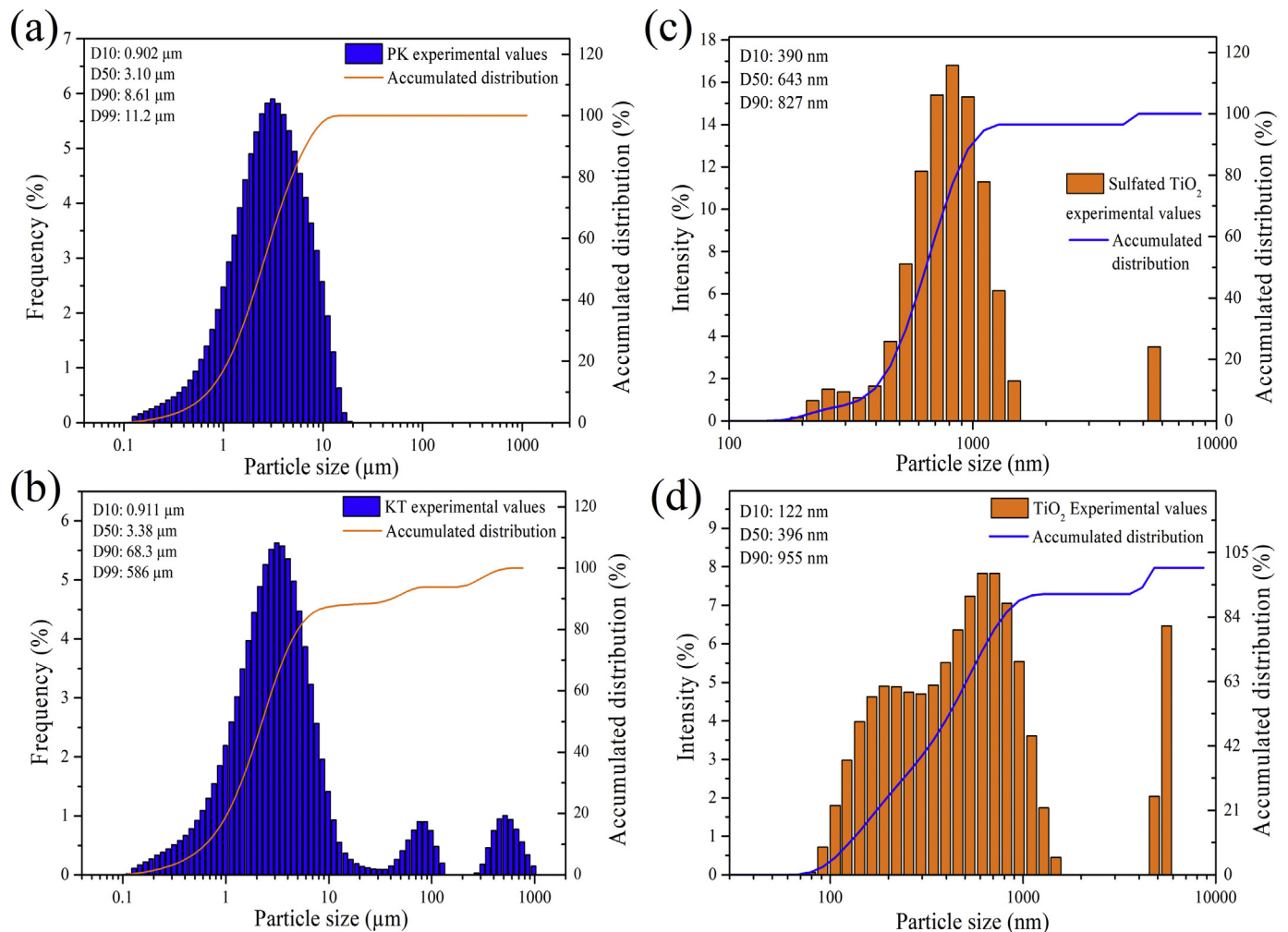


Fig. 6. (a) - Particle size distribution histogram of PK; (b) - Particle size distribution histogram of KT; (c) - Particle size distribution histogram of Sulfated TiO<sub>2</sub>; (d) - Particle size distribution histogram of AEROXIDE® TiO<sub>2</sub> P25.

orderly coagulation process begins due to the electrostatic attraction between of the different particles and the smaller particles promote the covering of the larger ones [80–82]. For this reason, the constant agitation of the reaction medium and high temperature is important to reduce these effects that are inherent in the process [83].

To evaluate the particle size of commercial TiO<sub>2</sub> and sulfated TiO<sub>2</sub>, distilled water was used. Fig. 6c and d shows the particle size histogram for titania, which has a bimodal profile that shows the presence of two representative average sizes at about 190 nm (peak 1) and 615 nm (peak 2). D10 showed that about 10% of the titania dispersed in a neutral aqueous medium has a size of up to 122 nm. D50 showed an average global size of around 396 nm and D90 reveals that 90% of the clusters have a diameter below 955 nm. For sulfated TiO<sub>2</sub>, the size of the agglomerates formed is similar for the values of D10, D50, and D90, showing that there are no significant differences for this characteristic between the materials.

### 3.1.7. XRD analyses

The average crystallite size ( $D_{001}$ ) of PK and KT was determined by analyzing X-ray diffractions of the planes K(001) and K(002) in  $2\theta$ . The reason for selecting these peaks was that it has the highest intensity among all kaolinite reflections (00l). The crystallite size was obtained using the X'Pert HighScore Plus software, based on the Debye-Scherrer equation (Eq. (5)), where  $D_{hkl}$  corresponds to the average crystallographic size in the h, k, l direction,  $K$  is the crystallite-shape factor (0.94 for “h, k, l = 0,0,1” reflections),  $\lambda$  is the wavelength of incident X-ray,  $\beta$  is the X-ray diffraction broadening (Full Width at Half-Maximum – FWHM, in radians), and  $\theta$  is the angle between the incident rays and the surface of the materials (Bragg angle) [84].

$$D_{hkl} = \frac{K \cdot \lambda}{\beta \cdot \cos\theta} \quad (5)$$

Interplanar distance between atoms ( $d$ ) was calculated using the Bragg's law (Eq. (6)), based on the position of (001), where  $n$  is a positive integer (1),  $\lambda$  is the X-ray wavelength, and  $\theta$  is the Bragg angle.

$$d = \frac{n \cdot \lambda}{2 \sin\theta} \quad (6)$$

Fig. 7a shows the XRD of PK, KT, and TiO<sub>2</sub>. The XRD analysis of AEROXIDE® TiO<sub>2</sub> P25 used to obtain KT, shows the peaks in  $2\theta$  of 25.25°, 27.31°, 36.96°, 47.99°, 53.97°, 55.00°, and 62.73° corresponding to planes A(101), R(110), A(004), A(200), A(105), A(211), and A(204) respectively [12]. The diffractogram suggests that the TiO<sub>2</sub> is composed of two phases, with about 78% corresponding to Anatase and 22% of

Rutile, these percentages are suggested by the analysis of diffractions carried out using X'Pert HighScore Plus software. According to the Debye-Scherrer equation (Eq. (5)), the average size of Anatase crystallite was about 18 nm and Rutile of about 6 nm. The XRD analysis revealed that pure kaolinite has a triclinic form (kaolinite-1A) that can be described as Al<sub>2</sub>Si<sub>2</sub>O<sub>5</sub>(OH)<sub>4</sub>, the kaolinite (K) peaks detected were 12.39°, 19.89°, 24.90°, 34.97°, 35.91°, 37.71°, and 38.47°. Respectively, these peaks refer to the K(001), K(110), K(002), K(130), K(200), K(003), and K(113) planes [1,12,72,85].

The diffractogram suggests that the PK sample is composed of a single-phase, with about 96% corresponding to kaolinite according to the software analysis. The d-spacing value for 12.39° (001) and 24.90° (002) in  $2\theta$  were 7.13 and 3.57 Å, in agreement with the literature. The average crystallite size calculated for PK was 39.66 nm. The XRD analysis of the KT composite identified kaolinite (about 84%) and titanium dioxide (about 14%) in the Anatase (about 11%) and Rutile (about 3%) phases, these results show that the proportions of the titania phases adhered to kaolinite are maintained. Kaolinite peaks were identified at 12.40°, 19.91°, 24.92°, 35.01°, 36.02°, 37.78°, and 38.49°, corresponding to the same planes identified in the PK sample with small displacements [1,12,43,72,85]. According to Shao et al. [1], the decrease in the intensity of the K(001) peak can be attributed to the presence of TiO<sub>2</sub> in the sample, as observed in 12.40° of KT when compared to the same PK plane.

Based on the FWHM values for the K(001) and K(002) peaks, the results found for PK were 0.2104 and 0.2402, respectively, while for KT, the values were 0.1644 and 0.1670. According to Hamzaoui et al. [85], this may indicate that kaolinite is closer to a more crystalline and orderly structure. The average crystallite size calculated for KT was 50.8 nm, which is larger than the crystallite size found for PK. This increase in crystallite size can be explained by the effects of acid pH on kaolinite in the reaction medium during the preparation of the composite. According to Awad et al. [84], the pH influences the size of the crystallites and the stacking of the layers, and in acidic conditions, the crystallization and the perfect stacking of the kaolinite layers are favored. The d-spacing for 12.40° (001) and 24.92° (002) in  $2\theta$  for KT, were respectively 7.12 and 3.57 Å, indicating that there was no change in kaolinite interplanar spacing, and therefore all impregnated material was limited to surface adhesion, i.e., intercalation processes were not observed, as expected. In the KT sample, peaks at 25.33°, 27.48°, 37.13°, 48.07°, 54.11°, 55.13° and 62.30° of  $2\theta$  were also identified, corresponding to the Anatase (A) and Rutile (R) phases of TiO<sub>2</sub>, A(101), R(110), A(004), A(200), A(105), A(211), and A(204) respectively [12]. The average crystallite size for TiO<sub>2</sub> in the KT sample was 19.07 nm.

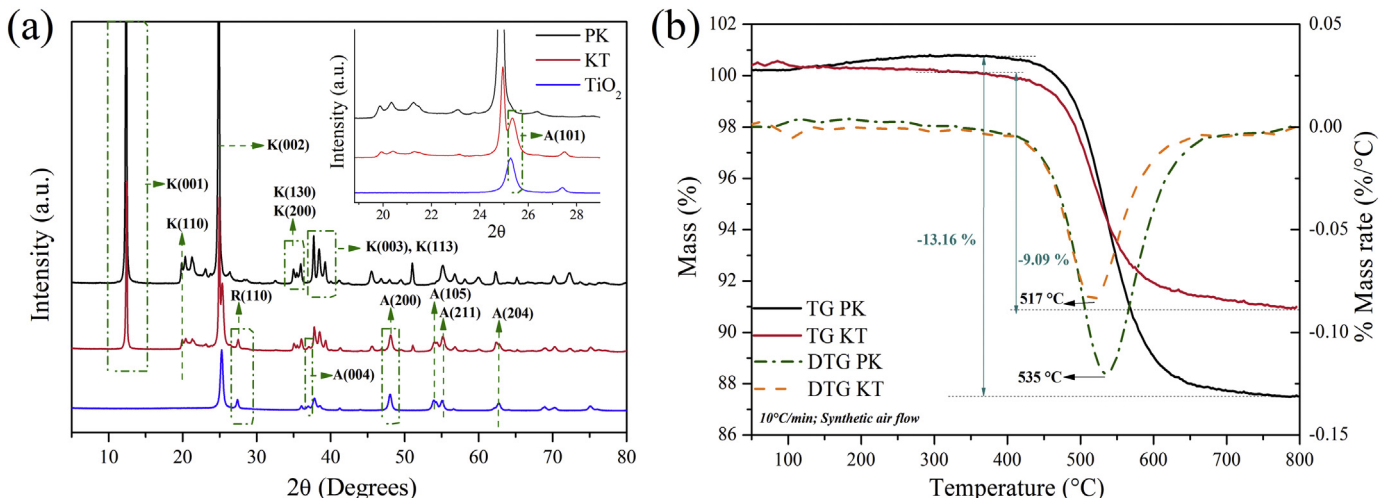
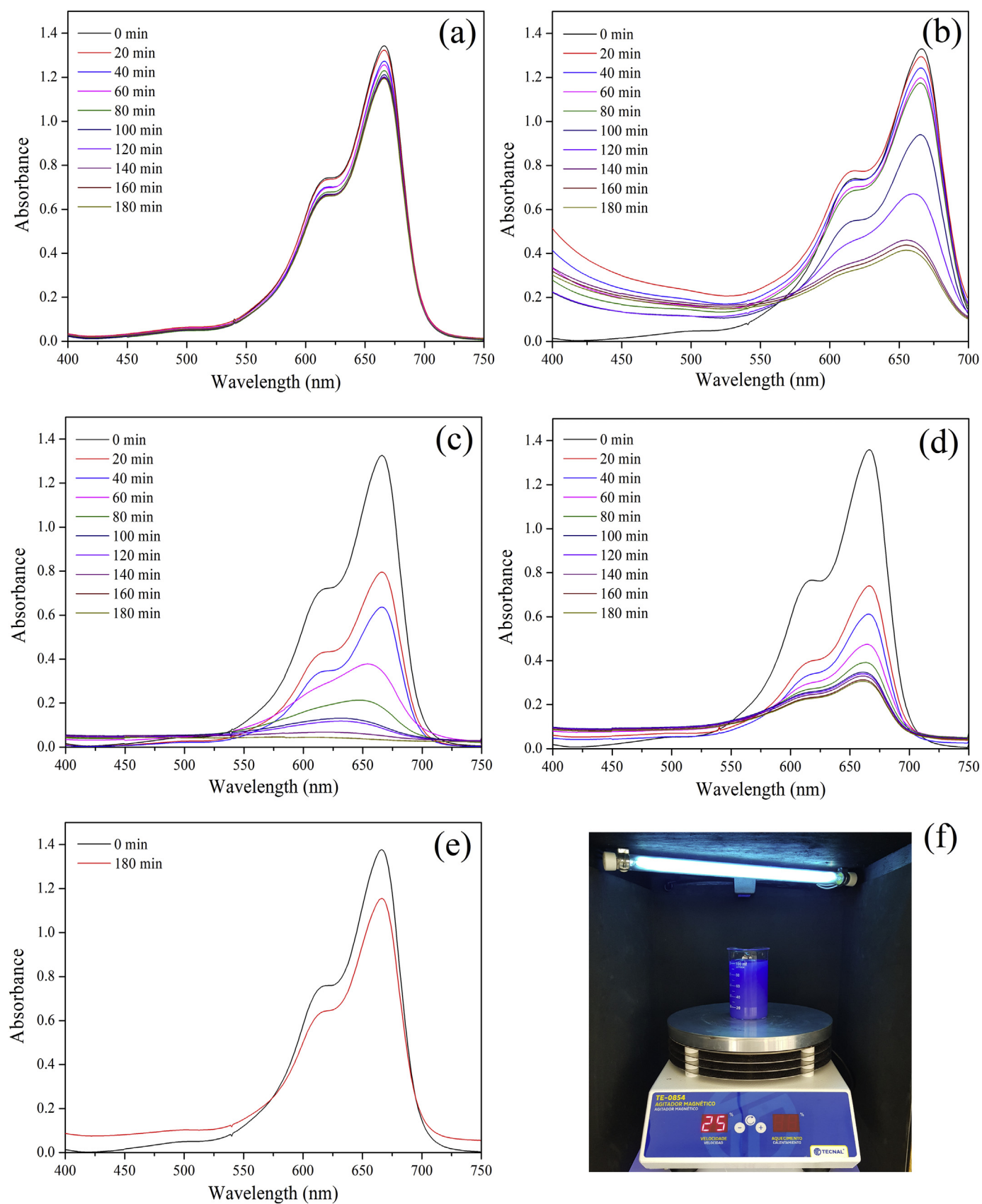


Fig. 7. (a) – XRD analysis of TiO<sub>2</sub>, KT composite, and PK. (b) – TGA-DTG analysis of KT composite, and



**Fig. 8.** Spectral curves of the photocatalytic degradation process of methylene blue (MB) dye. (a) – Photolysis; (b) – MB solution containing TiO<sub>2</sub> (AEROXIDE® TiO<sub>2</sub> P25); (c) – MB solution containing KT composite; (d) – MB solution containing KT\*; (e) – MB solution containing PK; (f) – Photoreactor system.

### 3.1.8. TGA-DTG analyses

TGA-DTG for the PK and KT particles are shown in Fig. 7b. At the beginning of the heating process until about 110 °C, a mass loss of about 2% was observed and a less pronounced peak can be seen in the DTG for PK and KT samples, which is related to its dehydration [43]. No mass loss was observed between 100 and 400 °C, which indicates an absence of water in the internal channels of the crystal [1,13,43] and the absence of organic matter and other contaminants [43,73,86]. A pronounced peak with a mass loss of around 13.8% and 10.1% for PK and KT, respectively, can be observed between 400 and 700 °C with a peak of maximum decomposition at 518 and 512 °C for PK and KT, respectively. This mass loss is related to dehydroxylation of kaolinite which leads to the formation of metakaolinite. The KT thermogram showed a slightly lower final mass loss compared to PK, related to the TiO<sub>2</sub> present on the composite surface.

### 3.2. Photocatalytic decomposition of methylene blue dye

Fig. 8 shows the spectral scan of the photocatalytic degradation kinetics of the MB solution. The spectral curves show slow photolysis that tends to stabilize after 3 h of exposure with a degradation efficiency of about 11% using only UV-C irradiation (Fig. 8a). Fig. 8b shows the photodegradation kinetic spectral curve of the MB solution containing free TiO<sub>2</sub> (AEROXIDE® TiO<sub>2</sub> P25). Photocatalysis with TiO<sub>2</sub> reached an efficiency of about 70% after 3 h of exposure. Fig. 8c shows

the photocatalytic process of the MB solution containing the KT composite. Among all the tested samples, the KT composite showed the best photocatalytic result with an efficiency of approximately 97% of dye degradation (Fig. 9a). The KT\* powder presented a good photocatalytic activity with an efficiency of about 78% of degradation, however, the spectral curves show a tendency to stabilize at about 3 h. Kaolinite alone (PK) did not show relevant photocatalytic activity during the 3 h exposure period as shown by the initial and final spectra presented in Fig. 8e.

The Langmuir–Hinshelwood model (Eq. (7)) takes the form of the pseudo-first-order kinetics model (Eq. (8)) for the photocatalytic degradation of a substrate at a low concentration ( $KC \ll 1$ ) [87–92]. Where  $C$  (mg/L) is the reactant concentration;  $r$  (mg /L·min) is the rate of MB oxidation at time  $t$  (min);  $K$  is the equilibrium constant for adsorption of MB on the surface of powder (catalyst); and  $k_r$  is the limiting rate constant, when the catalyst surface reaches maximum coverage. When  $C$  is very small, the product of  $KC$  is negligible so that integration of Eq. (7) between the conditions ( $t = 0; C_0$ ) and ( $t; C_t$ ) gives Eq. (8), that describes a first-order kinetics, where  $C_t$  is concentration after exposure to light at time  $t$  (min);  $C_0$  is the initial concentration (before photoreaction); and  $k_{app}$  corresponds to the product of  $k_r K$ , that is the apparent first-order reaction constant.

$$r = -\frac{dC}{dt} = \frac{k_r KC}{1 + KC} \quad (7)$$

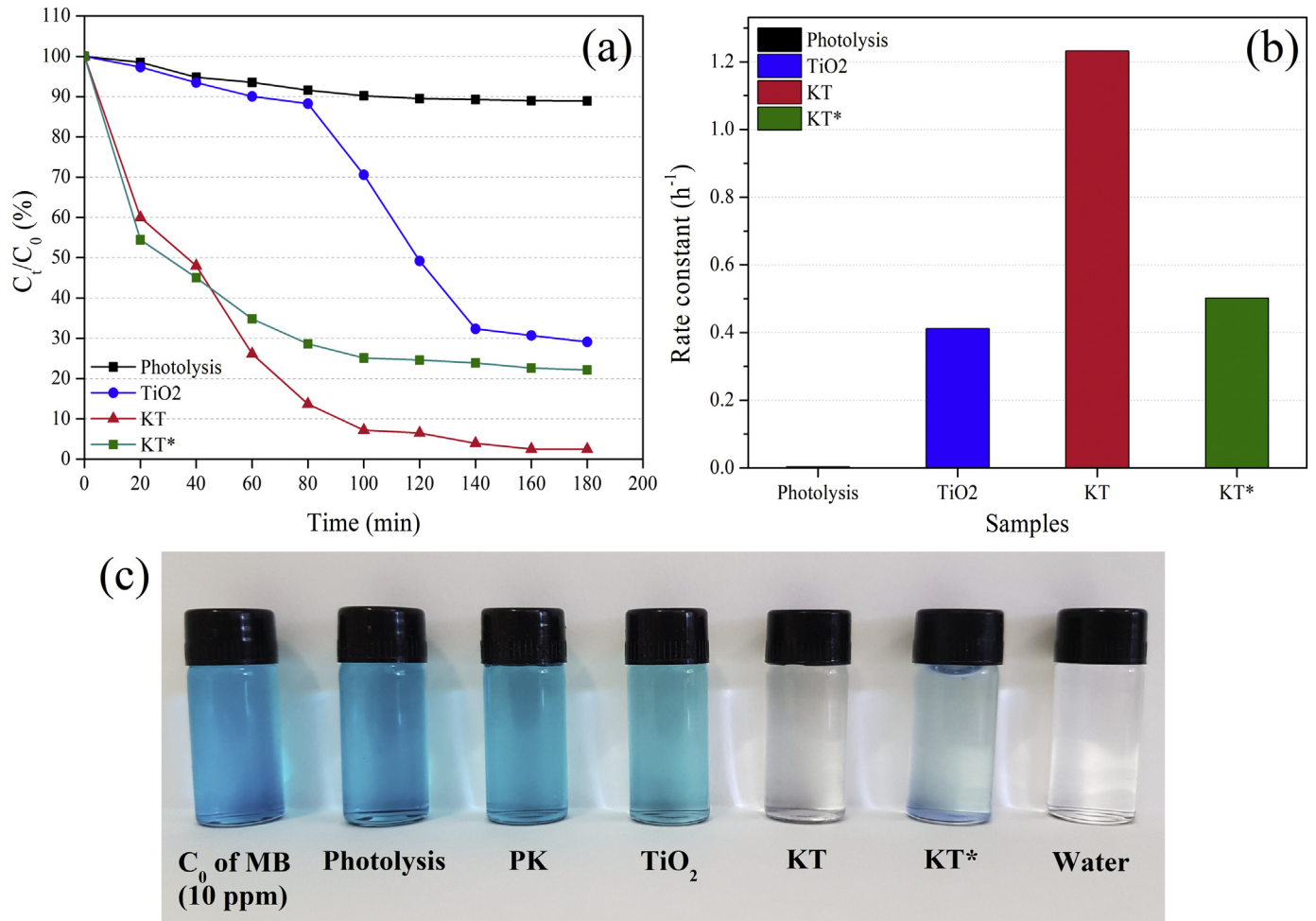


Fig. 9. (a) - Photodecomposition kinetics of methylene blue dye solution containing KT, KT\*, TiO<sub>2</sub> (AEROXIDE® TiO<sub>2</sub> P25), and by photolysis; (b) -  $k_{app}$  ( $h^{-1}$ ) of KT, KT\*, TiO<sub>2</sub> (AEROXIDE® TiO<sub>2</sub> P25), and photolysis in the MB photodegradation process; (c) - Color intensity of the solutions resulting from photodegradation after 3 h of exposure to UV-C light.

**Table 1**  
Results of the degradation photocatalytic process of methylene blue (MB).

Sample	C (%) - 1 h	C (%) - 2 h	C (%) - 3 h	$k_{app}$ (h <sup>-1</sup> )	Standard Error	R <sup>2</sup>	$P_{MB}$ (mol/m <sup>2</sup> ·h)	$\varphi_{\lambda}$ (%)
Photolysis	93.6	89.5	88.9	0.0039	0.00091	0.8801	–	5.3E-04
TiO <sub>2</sub>	90.1	49.2	29.1	0.412	0.00486	0.8805	16.546E-05	5.49E-03
KT	26.1	6.5	2.5	1.232	0.02867	0.9794	24.567E-05	1.63E-02
KT*	34.8	24.6	22.2	0.502	0.03976	0.8107	19.172E-05	6.84E-03

Legend: KT - Composite obtained from the reaction with sulfated TiO<sub>2</sub> sol-gel; KT\* - Composite obtained from the reaction with TiO<sub>2</sub> (without prior sulfation process); C (%) - Percentage concentration of MB at time t (h);  $k_{app}$  - Apparent first-order reaction rate constant; R<sup>2</sup> - Determination coefficient of fitness for Langmuir-Hinshelwood pseudo-first-order model;  $P_{MB}$  - Specific photocatalytic activity;  $\varphi_{\lambda}$  - Photonic efficiency, at 1 s. Note: Results are reported as "mean ± standard deviation" from two independent determinations.

$$-\ln\left(\frac{C_t}{C_0}\right) = k_{app}t \quad (8)$$

The  $k_{app}$  resulting from the linear plots by applying Eq. (8), are summarized in Table 1, as well as the values of the correlation coefficient (R<sup>2</sup>) for each photocatalyst tested. The KT composite showed the highest  $k_{app}$  value when compared to free TiO<sub>2</sub> and KT\*, therefore the photocatalytic degradation with KT, in addition to being more efficient, occurs more quickly than with the others. In this context, the order of degradation kinetics follows the sequence KT > KT\* > TiO<sub>2</sub>.

Specific photocatalytic activity ( $P_{MB}$ ) and photonic efficiency ( $\varphi_{\lambda}$ ) are the standard expressions of photoactivity according to ISO 10678:2010 [87–92]. The photocatalytic activity of the powders is calculated by the difference between the specific degradation rates (R) of the dye in the irradiated solution and the solution kept in the dark (blank). While photonic efficiency is an important factor that correlates the degradation efficiency of the irradiated sample to the amount of photon incident in the reactor for the decomposition of the dye. The specific degradation rate, R, was calculated from Eq. (9), where  $\Delta Abs$  is the difference between absorption measures during kinetics (dimensionless); V is the volume of the MB solution (m<sup>3</sup>);  $\Delta t$  is the time difference between the evaluated interval (h);  $\varepsilon$  is the molar extinction coefficient of MB at 664 nm, which is 7402.8 m<sup>2</sup>/mol; d is the measuring cell length used at the spectrophotometer (m), and A is the irradiated area of MB solution containing the photocatalyst (m<sup>2</sup>). R of the dark ( $R_{dark}$ ) and irradiated ( $R_{irr}$ ) samples makes it possible to calculate the specific photocatalytic activity by Eq. (10).

$$R = \frac{\Delta Abs \cdot V}{\Delta t \cdot \varepsilon \cdot d \cdot A} \quad (9)$$

$$P_{MB} = R_{irr} - R_{dark} \quad (10)$$

$$\varphi_{\lambda} = \frac{M}{L} \quad (11)$$

Finally, the photonic efficiency,  $\varphi_{\lambda}$ , can be calculated using Eq. (11), where M is the rate of decomposed molecules and L is the total rate of photons incident on the reactor. The number of MB molecules (for a volume of 100 mL) decomposed within time t is given by Eq. (12), where C<sub>0</sub> is the initial MB concentration (mol/L); N is the Avogadro's constant (6.023·10<sup>23</sup>/mol) and k is the apparent first-order reaction constant (s<sup>-1</sup>).

$$M_t = \left(\frac{100}{1000}\right) \cdot C_0 \cdot N \cdot (1 - e^{-kt}) \quad (12)$$

$$L_t = \frac{P \cdot \lambda \cdot t}{h \cdot c} \quad (13)$$

The number of incident photons within time t (s) is given by Eq. (13), where P is the light power (W);  $\lambda$  is the wavelength of light (m); h is the Planck's constant (6.63·10<sup>-34</sup> Js), c is the velocity of light in the vacuum (2.99·10<sup>8</sup> m/s). Considering a decomposition time as short as t = 1 s, the  $\varphi_{\lambda}$  corresponds to the "initial photonic efficiency".

Assuming that all incident photons are absorbed by the solid surface of the photocatalyst, then the values found constitutes a lower limit of the real quantum yield [87–92]. Therefore, Eqs. (11, 12, and 13) can help us to get a first approximation about the quantum efficiency of the decomposition process. It must be considered that the values of  $\varphi_{\lambda}$  found are not standardized, since the number of photons absorbed by the photocatalyst is experimentally difficult to measure. To compare the data reference, a test was performed with unsupported TiO<sub>2</sub> and KT\* which was prepared without previous sulfation of TiO<sub>2</sub>. The results in Table 1 show that  $k_{app}$ ,  $P_{MB}$ , and  $\varphi_{\lambda}$  follow the same magnitude behavior always in the KT > KT\* > TiO<sub>2</sub> sequence. Therefore, the KT composite is more effective in the MB photodegradation under the tested conditions than KT\* and the Free TiO<sub>2</sub>. This difference can be explained by the fact that photocatalysis is a surface phenomenon and requires direct contact between the dye and the photocatalyst. Therefore, it can be supposed that KT\* has less TiO<sub>2</sub> particles adhered to its surface than KT, and therefore has an intermediate yield. Fig. 9c shows the color intensity of the solutions after 3 h of exposure to light. The effect of the photodegradation of the dye solution containing KT is noticeable, which corroborates the values presented in Table 1.

### 3.3. Titania adhesion mechanism into the kaolinite from sulfated TiO<sub>2</sub> sol-gel

As previously mentioned, the KT composite preparation reaction takes place at a pH close to 1.0, i.e., under strongly acidic conditions due to the addition of sulfated TiO<sub>2</sub> to the reaction medium. Therefore, the Zeta Potential analysis used to investigate the electrochemical behavior of mineral particles as a function of pH, allowed an understanding of the possible interactions between the components of the reaction under acidic conditions. Zeta Potential of particles as a function of pH is shown in Fig. 2a. Regarding TiO<sub>2</sub>, it is possible to observe that for pH values below 6.0, the particles acquire a cationic character with an IEP between pH 6.0 and 6.5 whereas kaolinite is predominantly anionic for the entire pH range. However, in the presence of an electrolyte at lower pH, the negative surface charge decreases due to the electrostatic shielding caused by the counterions. It is known that in neutral conditions the kaolinite particles form different structures that directly depend on the surface charge of its faces and edges [45,49]. Thus, the Zeta Potential analysis presented reflects only the general magnitude of the particle surface, without differentiating the anionic (faces) and cationic (edges) zones, unlike other more refined techniques such as an electron spin resonance (ESR) spectrometer or an electrochemical analyzer to collect the electrochemical impedance spectroscopy (EIS) [77]. According to the proton adsorption model discussed in the work of Doi et al. [93], the adsorption sites on the kaolinite surface may include sites of permanent negative charge (basal planes) and the edge sites. However, the adsorption of divalent cations in the basal planes is insignificant due to the thermodynamically unfavorable performance of unspecified reactions of ion exchange in these locations. For Doi and coworkers, adsorption of cations at the edge sites is more favorable when complexation reactions occur on the surface. Considering the electrical properties of kaolinite, according to Gu and Evans [94],



## 4. Conclusions

The current research successfully presented a method for the development of a titanium precursor *via* sulfation of TiO<sub>2</sub> using concentrated sulfuric acid to obtain a sol-gel. The reaction product is a superacid solid with a strong cationic character capable of an ionic interaction with reactive sites that the clay mineral acquires in an acidic aqueous medium. Sulfated TiO<sub>2</sub> was obtained *via* hydrolytic reaction, and used as a sol-gel to obtain a kaolinite/TiO<sub>2</sub> composite. The analysis of Zeta Potential allowed an understanding of the possible interactions that occur between minerals in the pH range in which the reaction to obtain the composite occurs. The surface charge characteristics of the particles as a function of the pH changed with the sample. The XRD analysis of the KT composite showed peaks characteristic of both materials, indicating the presence of TiO<sub>2</sub> applied to the kaolinite, in the same way, changes in the thermal stability between PK and KT were observed through the TGA analysis. The material obtained showed two very characteristic phases, one of them referring to the matrix phase (kaolinite) and the other to the dispersed phase (TiO<sub>2</sub>). Both phases were easily identified in SEM-FEG and TEM morphological analyses and chemically identified in FTIR analysis. The thermal reinforcement of kaolinite by adhered titania can also be observed in the thermal analysis of TGA-DTG. Finally, the photocatalytic degradation test of the methylene blue solution containing the KT composite showed an efficiency of about 97% in the degradation of the dye. The values of specific photoactivity and photonic efficiency were also higher when compared to the results of the test with TiO<sub>2</sub>; KT\*, PK, and the effect of photolysis. Considering all the aspects mentioned, the material obtained in this work is characterized as a nano-hybrid composite, as proven by the micrographs and DLS analyses. Therefore, the composite obtained showed that sulfated TiO<sub>2</sub> is effective for this purpose and may indicate that its use as a precursor agent for titania is promising.

## Declaration of Competing Interest

None.

## Acknowledgments

This study was financed in part by the Coordenação de Aperfeiçoamento de Pessoal de Nível Superior (CAPES), Brazil - Finance Code 001. The authors are grateful to Federal University of Santa Catarina (UFSC), for the infrastructure of its laboratories to this research: Mass Transfer Laboratory (LABMASSA); Central Laboratory of Electronic Microscopy (LCME); Interdisciplinary Laboratory for the Development of Nanostructures (LINDEN); Laboratory of Separation Processes by Membrane (LABSEM); Process Control Laboratory (LCP); and the Chemical Engineering Analysis Center (CENTRAL-EQA).

## References

- [1] G.N. Shao, M. Engole, S.M. Imran, S.J. Jeon, H.T. Kim, Sol-gel synthesis of photoactive kaolinite-titania: effect of the preparation method and their photocatalytic properties, *Appl. Surf. Sci.* 331 (2015) 98–107, <https://doi.org/10.1016/j.apsusc.2014.12.199>.
- [2] M. Bensitel, O. Saur, J.C. Lavalley, B.A. Morrow, An infrared study of sulfated zirconia, *Mater. Chem. Phys.* 19 (1988) 147–156, [https://doi.org/10.1016/0254-0584\(88\)90007-7](https://doi.org/10.1016/0254-0584(88)90007-7).
- [3] T. Jin, T. Yamaguchi, K. Tanabe, Mechanism of acidity generation on sulfur-promoted metal oxides, *J. Phys. Chem.* 90 (1986) 4794–4796, <https://doi.org/10.1021/j100411a017>.
- [4] S.M. Pasini, A. Valério, S.M.A. Guelli Ulson de Souza, D. Hotza, G. Yin, J. Wang, A.A. Ulson de Souza, Plasma-modified TiO<sub>2</sub>/polyetherimide nanocomposite fibers for photocatalytic degradation of organic compounds, *J. Environ. Chem. Eng.* 7 (2019) 103213, <https://doi.org/10.1016/j.jece.2019.103213>.
- [5] M.N. Chong, B. Jin, C.W.K. Chow, C. Saint, Recent developments in photocatalytic water treatment technology: a review, *Water Res.* 44 (2010) 2997–3027, <https://doi.org/10.1016/j.watres.2010.02.039>.
- [6] J.K. Grewal, M. Kaur, Effect of core-shell reversal on the structural, magnetic and adsorptive properties of Fe<sub>2</sub>O<sub>3</sub>-GO nanocomposites, *Ceram. Int.* 43 (2017) 16611–16621, <https://doi.org/10.1016/j.ceramint.2017.09.051>.
- [7] M.A. de Bittencourt, A.M. Novack, J.A. Scherer Filho, L.P. Mazur, B.A. Marinho, A. da Silva, A.A.U. de Souza, S.M.A.G.U. de Souza, Application of FeCl<sub>3</sub> and TiO<sub>2</sub>-coated algae as innovative biophotocatalysts for Cr(VI) removal from aqueous solution: A process intensification strategy, *J. Clean. Prod.* 268 (2020) 122164, <https://doi.org/10.1016/j.jclepro.2020.122164>.
- [8] G.N. Shao, S.M. Imran, S.J. Jeon, M. Engole, N. Abbas, M. Salman Haider, S.J. Kang, H.T. Kim, Sol-gel synthesis of photoactive zirconia-titania from metal salts and investigation of their photocatalytic properties in the photodegradation of methylene blue, *Powder Technol.* 258 (2014) 99–109, <https://doi.org/10.1016/j.powtec.2014.03.024>.
- [9] G. Fu, P.S. Vary, C.-T. Lin, Anatase TiO<sub>2</sub> nanocomposites for antimicrobial coatings, *J. Phys. Chem. B* 109 (2005) 8889–8898, <https://doi.org/10.1021/jp0502196>.
- [10] A. Nakajima, K. Hashimoto, T. Watanabe, K. Takai, G. Yamauchi, A. Fujishima, Transparent superhydrophobic thin films with self-cleaning properties, *Langmuir* 16 (2000) 7044–7047, <https://doi.org/10.1021/ja000155k>.
- [11] X. Chen, S.S. Mao, Titanium dioxide nanomaterials: synthesis, properties, modifications and applications, *Chem. Rev.* 107 (2007) 2891–2959, <https://doi.org/10.1021/cr0500535>.
- [12] C. Wang, H. Shi, P. Zhang, Y. Li, Synthesis and characterization of kaolinite/TiO<sub>2</sub> nano-photocatalysts, *Appl. Clay Sci.* 53 (2011) 646–649, <https://doi.org/10.1016/j.clay.2011.05.017>.
- [13] K. Mamulová Kutlákova, J. Tokarský, P. Kovář, S. Vojtěšková, A. Kovářová, B. Smetana, J. Kukutschová, P. Čapková, V. Matějka, Preparation and characterization of photoactive composite kaolinite/TiO<sub>2</sub>, *J. Hazard. Mater.* 188 (2011) 212–220, <https://doi.org/10.1016/j.jhazmat.2011.01.106>.
- [14] D. Chen, H. Zhu, X. Wang, A facile method to synthesize the photocatalytic TiO<sub>2</sub> / montmorillonite nanocomposites with enhanced photoactivity, *Appl. Surf. Sci.* 319 (2014) 158–166, <https://doi.org/10.1016/j.apsusc.2014.05.085>.
- [15] Y. Xia, F. Li, Y. Jiang, M. Xia, B. Xue, Y. Li, Interface actions between TiO<sub>2</sub> and porous diatomite on the structure and photocatalytic activity of TiO<sub>2</sub>-diatomite, *Appl. Surf. Sci.* 303 (2014) 290–296, <https://doi.org/10.1016/j.apsusc.2014.02.169>.
- [16] R.M. de Almeida, L.K. Noda, N.S. Gonçalves, S.M.P. Meneghetti, M.R. Meneghetti, Transesterification reaction of vegetable oils, using superacid sulfated TiO<sub>2</sub>-base catalysts, *Appl. Catal. A Gen.* 347 (2008) 100–105, <https://doi.org/10.1016/j.apcata.2008.06.006>.
- [17] L.K. Noda, R.M. de Almeida, N.S. Gonçalves, L.F.D. Probst, O. Sala, TiO<sub>2</sub> with a high sulfate content—thermogravimetric analysis, determination of acid sites by infrared spectroscopy and catalytic activity, *Catal. Today* 85 (2003) 69–74, [https://doi.org/10.1016/S0920-5861\(03\)00195-0](https://doi.org/10.1016/S0920-5861(03)00195-0).
- [18] L.K. Noda, R.M. de Almeida, L.F.D. Probst, N.S. Gonçalves, Characterization of sulfated TiO<sub>2</sub> prepared by the sol-gel method and its catalytic activity in the n-hexane isomerization reaction, *J. Mol. Catal. A Gen.* 225 (2005) 39–46, <https://doi.org/10.1016/j.molcata.2004.08.025>.
- [19] R.M. De Almeida, Preparação e caracterização do TiO<sub>2</sub> sulfatado por algumas técnicas físico-químicas e sua utilização como catalisador em algumas reações., Universidade Federal de Santa Catarina, 2001. <https://repositorio.ufsc.br/bitstream/handle/123456789/94468/Rusiene Monteiro de Almeida.PDF?sequence=1>.
- [20] H. Makoto, K. Sakari, A. Kazushi, Reactions of Butane and Isobutane Catalyzed by Zirconium Oxide Treated with Sulfate Ion. *Solid Superacid Catalyst1*, *J. Am. Chem. Soc.* 101 (1979) 6439–6441, <https://doi.org/10.1021/ja00515a051>.
- [21] L.P. Hammett, A.J. Deyrup, A series of simple basic indicators. I. The acidity functions of mixtures of sulfuric and perchloric acids with water, *J. Am. Chem. Soc.* 54 (1932) 2721–2739, <https://doi.org/10.1021/ja01346a015>.
- [22] A. Zecchina, C. Lamberti, S. Bordiga, Surface acidity and basicity: general concepts, *Catal. Today* 41 (1998) 169–177, [https://doi.org/10.1016/S0920-5861\(98\)00047-9](https://doi.org/10.1016/S0920-5861(98)00047-9).
- [23] L.K. Noda, Superácidos: Uma Breve Revisão, *Quim Nova* 19 (1996) 135–147 [http://static.sites.sbgq.org.br/quimicanova.sbgq.org.br/pdf/Vol19No2\\_135\\_v19\\_n2\\_08.pdf](http://static.sites.sbgq.org.br/quimicanova.sbgq.org.br/pdf/Vol19No2_135_v19_n2_08.pdf).
- [24] N.F. Hall, J.B. Conant, A study of superacid solutions. I. The use of the chloranil electrode in glacial acetic acid and the strength of certain weak bases, *J. Am. Chem. Soc.* 49 (1927) 3047–3061, <https://doi.org/10.1021/ja01411a010>.
- [25] T. Yamaguchi, Recent progress in solid superacid, *Appl. Catal.* 61 (1990) 1–25, [https://doi.org/10.1016/S0166-9834\(00\)82131-4](https://doi.org/10.1016/S0166-9834(00)82131-4).
- [26] H. Armendariz, C. Sanchez Sierra, F. Figueras, B. Coq, C. Mirodatos, F. Lefebvre, D. Tichit, Hydrogen exchange between sulfated zirconias and per deuterio-benzene as characterization of the surface acidity: study by DRIFT and 1H MAS-NMR spectroscopies, *J. Catal.* 171 (1997) 85–92, <https://doi.org/10.1006/jcat.1997.1780>.
- [27] C. Li, Z. Sun, W. Zhang, C. Yu, S. Zheng, Highly efficient g-C<sub>3</sub>N<sub>4</sub>/TiO<sub>2</sub>/kaolinite composite with novel three-dimensional structure and enhanced visible light responding ability towards ciprofloxacin and *S. aureus*, *Appl. Catal. B Environ* 220 (2018) 272–282, <https://doi.org/10.1016/j.apcatb.2017.08.044>.
- [28] C. Li, X. Dong, N. Zhu, X. Zhang, S. Yang, Z. Sun, Y. Liu, S. Zheng, D.D. Dionysiou, Rational design of efficient visible-light driven photocatalyst through OD/2D structural assembly: natural kaolinite supported monodispersed TiO<sub>2</sub> with carbon regulation, *Chem. Eng. J.* 396 (2020) 125311, <https://doi.org/10.1016/j.cej.2020.125311>.
- [29] C. Li, N. Zhu, X. Dong, X. Zhang, T. Chen, S. Zheng, Z. Sun, Tuning and controlling photocatalytic performance of TiO<sub>2</sub>/kaolinite composite towards ciprofloxacin: role of OD/2D structural assembly, *Adv. Powder Technol.* 31 (2020) 1241–1252, <https://doi.org/10.1016/j.apt.2020.01.007>.
- [30] D. Kibanova, M. Trejo, H. Destaillets, J. Cervini-Silva, Synthesis of hectorite-TiO<sub>2</sub> and kaolinite-TiO<sub>2</sub> nanocomposites with photocatalytic activity for the degradation of model air pollutants, *Appl. Clay Sci.* 42 (2009) 563–568, <https://doi.org/10.1016/j.clay.2008.03.009>.
- [31] A. Nikokavoura, C. Trapalis, Alternative photocatalysts to TiO<sub>2</sub> for the photocatalytic reduction of CO<sub>2</sub>, *Appl. Surf. Sci.* 391 (2017) 149–174, <https://doi.org/10.1016/j.apsusc.2016.06.172>.

- [32] K.C. Nóbrega, A.S.D. Wanderley, A.M.D. Leite, E.M. Araújo, T.J.A. de Melo, Obtenção e caracterização de argilas organofílicas visando à aplicação em nanocompósitos poliméricos, *Rev. Eletrônica Mater. e Process.* 6 (2) (2011) 84–90 [www.dema.ufcg.edu.br/revista%0ARevista](http://www.dema.ufcg.edu.br/revista%0ARevista).
- [33] V.F. Melo, C.E.G.R. Schaefer, B. Singh, R.F. Novais, M.P.F. Fontes, Propriedades químicas e cristalográficas da caulinita e dos óxidos de ferro em sedimentos do grupo barreiras no município de Aracruz, estado do Espírito Santo, *Rev. Bras. Ciência Do Solo.* 26 (2002) 53–64, <https://doi.org/10.1590/s0100-06832002000100006>.
- [34] A.F. Baruel, R.C.L. Dutra, M.R. Baldan, C.M.A.L. Lopes, S.N. Cassu, *Organofiliação e Silanização de Argila Bentonita*, *Quim Nova* 41 (2018) 134–139.
- [35] G. Sposito, N.T. Skipper, R. Sutton, S.H. Park, A.K. Soper, J.A. Greathouse, Surface geochemistry of the clay minerals, *Proc. Natl. Acad. Sci. U. S. A.* 96 (1999) 3358–3364, <https://doi.org/10.1073/pnas.96.7.3358>.
- [36] A. Doi, M. Ejtemaei, A.V. Nguyen, Effects of ion specificity on the surface electrical properties of kaolinite and montmorillonite, *Miner. Eng.* 143 (2019) 105929, <https://doi.org/10.1016/j.mineng.2019.105929>.
- [37] H.H. Murray, Chapter 2 Structure and Composition of the Clay Minerals and their Physical and Chemical Properties, *Clay Miner* 2006, pp. 7–31, [https://doi.org/10.1016/S1572-4352\(06\)02002-2](https://doi.org/10.1016/S1572-4352(06)02002-2).
- [38] P. Leroy, A. Revil, A triple-layer model of the surface electrochemical properties of clay minerals, *J. Colloid Interface Sci.* 270 (2004) 371–380, <https://doi.org/10.1016/j.jcis.2003.08.007>.
- [39] C.R.S. de Oliveira, M.A. Batistella, L.A. Lourenço, S.M. de A.G.U. de Souza, A.A.U. de Souza, Cotton fabric finishing based on phosphate/clay mineral by direct-coating technique and its influence on the thermal stability of the fibers, *Prog. Org. Coatings* 150 (2021) 105949, <https://doi.org/10.1016/j.porgcoat.2020.105949>.
- [40] F. Bergaya, G. Lagaly, Chapter 1 general introduction: clays, clay minerals, and clay science, *Dev. Clay Sci.* 1 (2006) 1–18, [https://doi.org/10.1016/S1572-4352\(05\)01001-9](https://doi.org/10.1016/S1572-4352(05)01001-9).
- [41] P.V. Brady, R.T. Cygan, K.L. Nagy, Molecular controls on kaolinite surface charge, *J. Colloid Interface Sci.* 183 (1996) 356–364, <https://doi.org/10.1006/jcis.1996.0557>.
- [42] X. Liu, X. Lu, R. Wang, E.J. Meijer, H. Zhou, H. He, Atomic scale structures of interfaces between kaolinite edges and water, *Geochim. Cosmochim. Acta* 92 (2012) 233–242, <https://doi.org/10.1016/j.gca.2012.06.008>.
- [43] L.V. Barbosa, L. Marçal, E.J. Nassar, P.S. Calefi, M.A. Vicente, R. Trujillano, V. Rives, A. Gil, S.A. Korili, K.J. Ciuffi, E.H. De Faria, Kaolinite-titanium oxide nanocomposites prepared via sol-gel as heterogeneous photocatalysts for dyes degradation, *Catal. Today* 246 (2015) 133–142, <https://doi.org/10.1016/j.cattod.2014.09.019>.
- [44] ISO 10678:2010, Fine ceramics (advanced ceramics, advanced technical ceramics) – Determination of photocatalytic activity of surfaces in an aqueous medium by degradation of methylene blue, *Int. Organ. Stand.* – ISO. (2010) 12, <https://www.iso.org/standard/46019.html#:~:text=ISO10678%3A2010%20specifies%20a,degrade%20dissolved%20organic%20molecules%20on%20accessed%20October%2028,%202020.>
- [45] R.I. Jeldres, E.C. Piceros, W.H. Leiva, P.G. Toledo, N. Herrera, Viscoelasticity and yielding properties of flocculated kaolinite sediments in saline water, *Colloids Surfaces A Physicochem. Eng. Asp.* 529 (2017) 1009–1015, <https://doi.org/10.1016/j.colsurfa.2017.07.006>.
- [46] T. Jiang, G.J. Hirasaki, C.A. Miller, Characterization of kaolinite  $\zeta$  potential for interpretation of wettability alteration in diluted bitumen emulsion separation, *Energy Fuels* 24 (2010) 2350–2360, <https://doi.org/10.1021/ef900999h>.
- [47] X. Chen, Y. Peng, Managing clay minerals in froth flotation—a critical review, *Miner. Process. Extr. Metall. Rev.* 39 (2018) 289–307, <https://doi.org/10.1080/08827508.2018.1433175>.
- [48] B. Derakhshandeh, Kaolinite suspension as a model fluid for fluid dynamics studies of fluid fine tailings, *Rheol. Acta* 55 (2016) 749–758, <https://doi.org/10.1007/s00397-016-0949-0>.
- [49] P.I. Au, Y.K. Leong, Rheological and zeta potential behaviour of kaolin and bentonite composite slurries, *Colloids Surfaces A Physicochem. Eng. Asp.* 436 (2013) 530–541, <https://doi.org/10.1016/j.colsurfa.2013.06.039>.
- [50] P. Shankar, J. Teo, Y.K. Leong, A. Fourie, M. Fahey, Adsorbed phosphate additives for interrogating the nature of interparticle forces in kaolin clay slurries via rheological yield stress, *Adv. Powder Technol.* 21 (2010) 380–385, <https://doi.org/10.1016/j.apt.2010.02.013>.
- [51] Y.K. Leong, J. Teo, E. Teh, J. Smith, J. Widjaja, J.X. Lee, A. Fourie, M. Fahey, R. Chen, Controlling attractive interparticle forces via small anionic and cationic additives in kaolin clay slurries, *Chem. Eng. Res. Des.* 90 (2012) 658–666, <https://doi.org/10.1016/j.cherd.2011.09.002>.
- [52] Q. Zhang, Z. Yan, J. Ouyang, Y. Zhang, H. Yang, D. Chen, Chemically modified kaolinite nanolayers for the removal of organic pollutants, *Appl. Clay Sci.* 157 (2018) 283–290, <https://doi.org/10.1016/j.clay.2018.03.009>.
- [53] D.L. Liao, G.S. Wu, B.Q. Liao, Zeta potential of shape-controlled TiO<sub>2</sub> nanoparticles with surfactants, *Colloids Surfaces A Physicochem. Eng. Asp.* 348 (2009) 270–275, <https://doi.org/10.1016/j.colsurfa.2009.07.036>.
- [54] G. Xu, J. Zhang, G. Li, G. Song, Effect of complexation on the zeta potential of titanium dioxide dispersion, *J. Dispers. Sci. Technol.* 24 (2003) 527–535, <https://doi.org/10.1081/DIS-120021807>.
- [55] S. Lebrétte, C. Pagnoux, P. Abéard, Stability of aqueous TiO<sub>2</sub> suspensions: influence of ethanol, *J. Colloid Interface Sci.* 280 (2004) 400–408, <https://doi.org/10.1016/j.jcis.2004.07.033>.
- [56] A. Zielińska-Jurek, Z. Bielan, S. Dudziak, I. Wolak, Z. Sobczak, T. Klimczuk, G. Nowaczyk, J. Hupka, Design and application of magnetic photocatalysts for water treatment. The effect of particle charge on surface functionality, *Catalysts* 7 (2017) <https://doi.org/10.3390/catal7120360>.
- [57] M.M. Ba-Abbad, A.A.H. Kadhum, A.B. Mohamad, M.S. Takriff, K. Sopian, Synthesis and catalytic activity of TiO<sub>2</sub> nanoparticles for photochemical oxidation of concentrated chlorophenols under direct solar radiation, *Int. J. Electrochem. Sci.* 7 (2012) 4871–4888.
- [58] M. Al-Amin, S. Chandra Dey, T.U. Rashid, M. Ashaduzzaman, S.M. Shamsuddin, Solar assisted Photocatalytic degradation of reactive Azo dyes in presence of Anatase titanium dioxide, *Int. J. Latest Res. Eng. Technol.* 2 (2016) 14–21 [www.ijlret.com](http://www.ijlret.com).
- [59] R.L. Ledoux, Infrared studies of the hydroxyl groups in intercalated kaolinite complexes, *Clay Clay Miner.* 13 (1964) 289–315, <https://doi.org/10.1346/CCMN.1964.0130128>.
- [60] A.C. Hess, V.R. Saunders, Periodic ab initio Hartree-Fock calculations of the low-symmetry mineral kaolinite, *J. Phys. Chem.* 96 (1992) 4367–4374, <https://doi.org/10.1021/j100190a047>.
- [61] M. Valášková, M. Rieder, V. Matějka, P. Čapková, A. Sliva, Exfoliation/delamination of kaolinite by low-temperature washing of kaolinite-urea intercalates, *Appl. Clay Sci.* 35 (2007) 108–118, <https://doi.org/10.1016/j.clay.2006.07.001>.
- [62] É. Makó, Z. Senkár, J. Kristóf, V. Vágvölgyi, Surface modification of mechanochemically activated kaolinites by selective leaching, *J. Colloid Interface Sci.* 294 (2006) 362–370, <https://doi.org/10.1016/j.jcis.2005.07.033>.
- [63] W. Zheng, J. Zhou, Z. Zhang, L. Chen, Z. Zhang, Y. Li, N. Ma, P. Du, Formation of intercalation compound of kaolinite-glycine via displacing guest water by glycine, *J. Colloid Interface Sci.* 432 (2014) 278–284, <https://doi.org/10.1016/j.jcis.2014.06.016>.
- [64] B.D. Mistry, *A Handbook of Spectroscopic Data - Chemistry*, 2009.
- [65] B.J. Saikia, G. Parthasarathy, R.R. Borah, R. Borthakur, Raman and FTIR spectroscopic evaluation of clay minerals and estimation of metal contaminations in natural deposition of surface sediments from Brahmaputra River, *Int. J. Geosci.* 07 (2016) 873–883, <https://doi.org/10.4236/ijg.2016.77064>.
- [66] J.T. Klopogge, *Raman Spectroscopy of Clay Minerals*, 1st ed Elsevier Ltd., 2017 <https://doi.org/10.1016/B978-0-08-100355-8.00006-0>.
- [67] R.L. Frost, The structure of the kaolinite minerals – a FT-Raman study, *Clay Miner.* 32 (1997) 65–77, <https://doi.org/10.1180/claymin.1997.032.1.08>.
- [68] Y. Zhang, Q. Liu, J. Xiang, S. Zhang, R.L. Frost, Insight into morphology and structure of different particle sized kaolinites with same origin, *J. Colloid Interface Sci.* 426 (2014) 99–106, <https://doi.org/10.1016/j.jcis.2014.03.057>.
- [69] S. Shoval, G. Panczer, M. Boudeulle, Study of the occurrence of titanium in kaolinites by micro-Raman spectroscopy, *Opt. Mater. (Amst.)* 30 (2008) 1699–1705, <https://doi.org/10.1016/j.optmat.2007.11.012>.
- [70] L. Qian, Z.L. Du, S.Y. Yang, Z.S. Jin, Raman study of titania nanotube by soft chemical process, *J. Mol. Struct.* 749 (2005) 103–107, <https://doi.org/10.1016/j.molstruc.2005.04.002>.
- [71] E.H. Alsharaeh, T. Bora, A. Soliman, F. Ahmed, G. Bharath, M.G. Ghoniem, K.M. Abu-Salah, J. Dutta, Sol-gel-assisted microwave-derived synthesis of anatase Ag/TiO<sub>2</sub>/Go nanohybrids toward efficient visible light phenol degradation, *Catalysts* 7 (2017) 1–11, <https://doi.org/10.3390/catal7050133>.
- [72] Y. Zhang, H. Gan, G. Zhang, A novel mixed-phase TiO<sub>2</sub>/kaolinite composites and their photocatalytic activity for degradation of organic contaminants, *Chem. Eng. J.* 172 (2011) 936–943, <https://doi.org/10.1016/j.cej.2011.07.005>.
- [73] H. Cheng, Q. Liu, J. Yang, S. Ma, R.L. Frost, The thermal behavior of kaolinite intercalation complexes—a review, *Thermochim. Acta* 545 (2012) 1–13, <https://doi.org/10.1016/j.tca.2012.04.005>.
- [74] E.H. de Faria, O.J. Lima, K.J. Ciuffi, E.J. Nassar, M.A. Vicente, R. Trujillano, P.S. Calefi, Hybrid materials prepared by interlayer functionalization of kaolinite with pyridine-carboxylic acids, *J. Colloid Interface Sci.* 335 (2009) 210–215, <https://doi.org/10.1016/j.jcis.2009.03.067>.
- [75] J.E. Gardolinski, Interlayer Grafting and Delamination of Kaolinite, Christian-Albrechts-University in Kiel, 2005 [https://macau.uni-kiel.de/servlets/MCRFileNodeServlet/dissertation\\_derivate\\_00001508/d1508.pdf](https://macau.uni-kiel.de/servlets/MCRFileNodeServlet/dissertation_derivate_00001508/d1508.pdf).
- [76] Y. Hai, X. Li, H. Wu, S. Zhao, W. Deligeer, S. Asuha, Modification of acid-activated kaolinite with TiO<sub>2</sub> and its use for the removal of azo dyes, *Appl. Clay Sci.* 114 (2015) 558–567, <https://doi.org/10.1016/j.clay.2015.07.010>.
- [77] C. Li, Z. Sun, X. Dong, S. Zheng, D.D. Dionysiou, Acetic acid functionalized TiO<sub>2</sub>/kaolinite composite photocatalysts with enhanced photocatalytic performance through regulating interfacial charge transfer, *J. Catal.* 367 (2018) 126–138, <https://doi.org/10.1016/j.jcat.2018.09.001>.
- [78] S. Lei, W. Gong, C. Bai, Y. Qu, Y. Gu, B. Xiong, C. Wang, Preparation of TiO<sub>2</sub>/kaolinite nanocomposite and its photocatalytic activity, *J. Wuhan Univ. Technol. Mater. Sci. Ed.* 21 (2006) 12–15, <https://doi.org/10.1007/BF02841194>.
- [79] J. Tokarský, P. Čapková, J.V. Burda, Structure and stability of kaolinite/TiO<sub>2</sub> nanocomposite: DFT and MM computations, *J. Mol. Model.* 18 (2012) 2689–2698, <https://doi.org/10.1007/s00894-011-1278-y>.
- [80] M.O. Carlos, J.R. Garcia, I.R. Oliveira, R. Salomão, V.C. Pandolfelli, Heterocoagulação como técnica para obtenção de cerâmicas porosas, *Cerâmica* 51 (2005) 78–84, <https://doi.org/10.1590/s0366-69132005000200002>.
- [81] F. Tang, H. Fudouzi, T. Uchikoshi, Y. Sakka, Preparation of porous materials with controlled pore size and porosity, *J. Eur. Ceram. Soc.* 24 (2004) 341–344, [https://doi.org/10.1016/S0955-2219\(03\)00223-1](https://doi.org/10.1016/S0955-2219(03)00223-1).
- [82] F. Tang, H. Fudouzi, Y. Sakka, Fabrication of macroporous alumina with tailored porosity, *J. Am. Ceram. Soc.* 86 (2003) 2050–2054, <https://doi.org/10.1111/j.1151-2916.2003.tb03607.x>.
- [83] P.W. Ratke, Voorhees Lorenz, Growth and Coarsening: Ostwald Ripening in Material Processing, 1st ed., 2002 <https://doi.org/10.1007/978-3-662-04884-9>.
- [84] M.E. Awad, A. López-Galindo, R. Sánchez-Espejo, C.I. Sainz-Díaz, M.M. El-Rahmany, C. Vieras, Crystallite size as a function of kaolinite structural order-disorder and kaolin chemical variability: Sedimentological implication, *Appl. Clay Sci.* 162 (2018) 261–267, <https://doi.org/10.1016/j.clay.2018.06.027>.
- [85] R. Hamzaoui, O. Bouchenafa, O. Ben Maaouia, S. Guessasma, Introduction of milled kaolinite obtained by mechanochemical synthesis to cement mixture for the production of

- mortar: study of mechanical performance of modified mortar, *Powder Technol.* 355 (2019) 340–348, <https://doi.org/10.1016/j.powtec.2019.07.062>.
- [86] H. Cheng, J. Yang, Q. Liu, J. He, R.L. Frost, Thermogravimetric analysis–mass spectrometry (TG-MS) of selected Chinese kaolinites, *Thermochim. Acta* 507–508 (2010) 106–114, <https://doi.org/10.1016/j.tca.2010.05.007>.
- [87] R.M. Sánchez-Albores, B.Y. Pérez-Sariñana, C.A. Meza-Avendaño, P.J. Sebastian, O. Reyes-Vallejo, J.B. Robles-Ocampo, Hydrothermal synthesis of bismuth vanadate-alumina assisted by microwaves to evaluate the photocatalytic activity in the degradation of methylene Blue, *Catal. Today* 353 (2020) 126–133, <https://doi.org/10.1016/j.cattod.2019.07.044>.
- [88] D.S. Tsoukleris, A.I. Kontos, P. Aloupogiannis, P. Falaras, Photocatalytic properties of screen-printed titania, *Catal. Today* 124 (2007) 110–117, <https://doi.org/10.1016/j.cattod.2007.03.029>.
- [89] V.R. Chelli, S. Chakraborty, A.K. Golder, Ag-doping on TiO<sub>2</sub> using plant-based glycosidic compounds for high photonic efficiency degradative oxidation under visible light, *J. Mol. Liq.* 271 (2018) 380–388, <https://doi.org/10.1016/j.molliq.2018.08.140>.
- [90] B. Szczepanik, Photocatalytic degradation of organic contaminants over clay-TiO<sub>2</sub> nanocomposites: a review, *Appl. Clay Sci.* 141 (2017) 227–239, <https://doi.org/10.1016/j.clay.2017.02.029>.
- [91] A. Wu, D. Wang, C. Wei, X. Zhang, Z. Liu, P. Feng, X. Ou, Y. Qiang, H. Garcia, J. Niu, A comparative photocatalytic study of TiO<sub>2</sub> loaded on three natural clays with different morphologies, *Appl. Clay Sci.* 183 (2019) 105352, <https://doi.org/10.1016/j.clay.2019.105352>.
- [92] A.L. da Silva, M. Dondi, D. Hotza, Self-cleaning ceramic tiles coated with Nb<sub>2</sub>O<sub>5</sub>-doped-TiO<sub>2</sub> nanoparticles, *Ceram. Int.* 43 (2017) 11986–11991, <https://doi.org/10.1016/j.ceramint.2017.06.049>.
- [93] A. Doi, M. Khosravi, M. Ejtemaei, T.A.H. Nguyen, A.V. Nguyen, Specificity and affinity of multivalent ions adsorption to kaolinite surface, *Appl. Clay Sci.* 190 (2020) <https://doi.org/10.1016/j.clay.2020.105557>.
- [94] X. Gu, L.J. Evans, Surface complexation modelling of Cd(II), Cu(II), Ni(II), Pb(II) and Zn(II) adsorption onto kaolinite, *Geochim. Cosmochim. Acta* 72 (2008) 267–276, <https://doi.org/10.1016/j.gca.2007.09.032>.
- [95] M. Tokarčíková, J. Tokarský, K. Čabanová, V. Matějka, K. Mamulová Kutláková, J. Seidlerová, The stability of photoactive kaolinite/TiO<sub>2</sub> composite, *Compos. Part B Eng.* 67 (2014) 262–269, <https://doi.org/10.1016/j.compositesb.2014.07.009>.
- [96] K.G. Bhattacharyya, S. Sen Gupta, Adsorption of a few heavy metals on natural and modified kaolinite and montmorillonite: a review, *Adv. Colloid Interf. Sci.* 140 (2008) 114–131, <https://doi.org/10.1016/j.cis.2007.12.008>.
- [97] S.L. Bee, M.A.A. Abdullah, M. Mamat, S.T. Bee, L.T. Sin, D. Hui, A.R. Rahmat, Characterization of silylated modified clay nanoparticles and its functionality in PMMA, *Compos. Part B Eng.* 110 (2017) 83–95, <https://doi.org/10.1016/j.compositesb.2016.10.084>.